

MnO_x catalysts supported on SBA-15 and MCM-41 silicas for a competitive VOCs mixture oxidation: *In-situ* DRIFTS investigations

E.J. Moreno-Román^a, F. Can^b, V. Meille^a, N. Guilhaume^a, J. González-Cobos^{a,*}, S. Gil^{a,*}

^a Univ Lyon, Université Lyon 1, CNRS, UMR 5256, IRCELYON, 2 avenue Albert Einstein, Villeurbanne F-69622, France

^b Institut de Chimie des Milieux et Matériaux de Poitiers (IC2MP), University of Poitiers, CNRS UMR 7285, TSA51106 – F86073, Poitiers Cedex 9, France

ARTICLE INFO

Keywords:
Supported MnO_x catalysts
MCM-41
SBA-15
VOCs binary mixture
In-situ DRIFTS

ABSTRACT

The catalytic oxidation of different volatile organic compounds (VOCs) has been widely studied for several decades within the field of air depollution. However, there is still much to understand regarding the effects that these VOCs have on each other when they are blended together in the reaction mixture, as would be expected in many emissions. Herein, the catalytic oxidation of toluene and 2-propanol on supported manganese oxides under both single and binary VOCs oxidation conditions has been studied. We have found the catalyst activity for VOCs mineralization and its selectivity towards other by-products (i.e., acetone or propylene from 2-propanol) to be strongly dependent on the reaction conditions, the catalyst redox properties and support acidity. We have also assessed the promotion/inhibition effects derived from the VOCs mixture and proposed the reaction mechanism in each case by means of *in-situ* DRIFTS measurements.

1. Introduction

In the last decades, air purification has become a public concern and an important research topic. Volatile organic compounds (VOCs) are recognized as main contributors to air pollution. Many of them are toxic and some are considered to be carcinogenic, mutagenic or teratogenic [1]. Furthermore, those pollutants are considered as the main precursors for particulate matter and ozone formation via photochemical reactions [2]. VOCs are emitted by several sources, including outdoor sources (transportation, industrial and energetic processes) and indoor sources (e.g., household products, construction materials, furniture and combustion by-products). The vast majority of emitted VOCs consists of compounds containing alkanes, esters, alkynes, aldehydes, aromatics and alcohols, and their environmental impact is typically dependent on the functionality [3]. Among the VOCs, toluene is mostly used as solvent in the chemical industry and the main contributor to photochemical smog formation. On the other hand, 2-propanol (iPrOH) is mainly used as a solvent in many industries such as building materials, petroleum refineries, textile, pesticides, pharmaceutical and body care industries [2], and it may be emitted from the same emissions sources as toluene [3].

VOCs emissions have been heavily regulated since 1999 by the European Union (EU). The Goteborg protocol modified in 2012 proposes

that EU countries must reduce the pollutants by 2030 [4]. To address this problem, several non-destructive techniques have been investigated and applied, including adsorption, condensation and membrane separation [5]. However, in practical applications, these techniques presented many disadvantages, due to their high initial capital investment, high VOCs concentration requirements, harsh operating conditions and high costs. Hence, alternative techniques have been applied for elimination/control of VOCs compounds such as thermal incineration and catalytic oxidation. The latter has been considered the most promising for abatement of VOCs, since it can burn them at temperatures around c. a. 200–500 °C, with high, medium and low concentrations, into CO₂ and H₂O [6].

Due to the merits of the catalytic oxidation, many investigations have been applied for the design and synthesis of catalysts for VOCs oxidation. Generally, noble-metal catalysts such as Au, Ag, Pt, Pd and Rh have exhibited high catalytic activities for VOCs mineralization and have been widely applied in the industrial processes [7]. In general, the catalytic activity depends on the nature of the noble metal and the VOC. For instance, Papaefthimiou et al. [8] studied different VOCs oxidation on Pt and Pd over Al₂O₃ catalysts. They demonstrated that Pt and especially Pd were active for benzene and butanol oxidation, while ethyl acetate was more difficult to oxidize. In addition, He et al. [9] investigated the efficiency of VOCs (toluene, benzene and ethyl acetate) oxidation over

* Corresponding authors.

E-mail addresses: jesus.gonzalez-cobos@ircelyon.univ-lyon1.fr (J. González-Cobos), sonia.gil@ircelyon.univ-lyon1.fr (S. Gil).



different supported Pd catalysts and they found the performance to decrease in the following order: Pd/ZSM-5 > Pd/SBA-15 > Pd/MCM-48 > Pd/MCM-41. In this study, the authors claimed that the performance was influenced by the acidity of the support, which would favour the active sites dispersion and CO₂ desorption from the catalysts. However, the low thermal stability, high manufacturing costs and high poisoning tendency of the noble metals limit their lifetime and implementation. Hence, non-noble metals oxides such as MnO_x, FeO_x, CuO_x, CoO_x with advantageous properties in these regards, with respect to the noble-metals catalysts [10,11]. Among all the transition-metal catalysts, MnO_x catalysts have demonstrated an excellent performance for single VOC oxidation [12,13].

Thus, MnO_x has been selected in the present study as a suitable active phase for synthesis of supported MnO_x catalysts. Indeed, the support can positively change the catalyst properties, improving dispersion but also preventing sintering [14,15]. Moreover, the use of a porous support can even improve the accessibility of reactants to the active sites, which greatly enhances the catalytic performance [15,16]. For instance, Kantzer et al. [14] and Li et al. [15] demonstrated that the dispersion of the MnO_x nanoparticles is clearly influenced by the support (CeO₂-ZrO₂ or WO₃-TiO₂ and HZSM-5, respectively), improving the redox and surface properties of the resultant supported MnO_x catalysts. The improvement in above-mentioned properties was correlated to the enhanced catalytic activity for VOCs oxidation [14,15]. Si et al. [16] also showed that the properties of the support, notably the textural properties (e.g. specific surface area, morphology, pore structure, etc.), had an important influence on catalytic activity for VOCs removal. Thus, the supported MnO_x catalysts with higher specific surface area and abundant nanopores presented higher catalytic activity for toluene oxidation, which has been associated to the improved contact area and accessibility of toluene to the active sites. In addition, Cao et al. [17] showed that the structural properties of CeO₂ support like the morphology (nanosphere, nanorod, nanocube) had an important impact on MnO_x sintering and thermal stability of supported MnO_x catalysts, which are the key factor to ensure the catalytic activity for VOCs. Interestingly, these authors attributed the improved sintering resistance of spherical MnO_x/CeO₂ catalysts to the confinement effect generated by the support porosity, protecting MnO_x nanoparticles, which are trapped into the nanopores presented in spherical support. Finally, Zhang et al. [18] attributed the higher catalytic activity for toluene removal of MnO_x/SiO₂ catalyst to the positive interaction between MnO_x and porous silica support, which promotes the spillover of active surface oxygen species. About all, the design of supported MnO_x catalysts seems to be a promising strategy to improve the performance regarding the catalytic oxidation of VOCs.

Moreover, industrial exhaust gases does not present a single VOC but a mixture of VOCs with different chemical character, such as aromatic hydrocarbons, alkanes, oxy-derivatives or halogenated compounds [2, 19–23]. For this reason, few studies have been focused on the mixture oxidation reaction. Other authors have found inhibition and promotion effects in comparison with the single VOC oxidation reaction [2,19–23]. A promotional effect in the binary toluene and iPrOH mixture has been observed in our previous work using bulk manganese oxide catalysts [2], which was attributed to the different polarity of the VOCs, the available surface oxygen and the exothermic character provided by the VOCs simultaneous oxidation reaction. A promoting effect on toluene oxidation was also observed by Pan et al. [24] during the oxidation of acetone and/or ethyl acetate over MnO_x catalysts. They observed that the presence of both compounds in the reaction media promotes the formation of toluene intermediates, which enhanced its conversion at low temperature. In addition, they also showed an activation at low temperature due to the exothermic phenomena provided by the oxidation of the other VOCs presented in the mixture. The exothermic character was also observed by Burgos et al. [25]. They showed that the complete oxidation of toluene and methyl ethyl ketone (MEK) was not affected in the presence of iPrOH on Pt/Al₂O₃/Al monoliths. Nonetheless, the presence of toluene inhibits the dehydrogenation of iPrOH to acetone but

promotes the completely oxidation of acetone at lower temperatures due to the exothermic phenomena mentioned above. Other inhibition effects were also observed in the literature. Ordóñez et al. [26] and Wang et al. [19] studied binary mixtures of different VOCs including toluene over Pt/γ-Al₂O₃ and Pt/TiO₂ catalysts, where the VOCs competed for the active sites caused leading to the inhibiting effect in the mixture oxidation. In the same way, the competitive adsorption between iPrOH and o-xylene was also observed in literature [22], showing a strong inhibition of iPrOH by o-xylene over NaX zeolites. Indeed, the simultaneous presence of both compounds and, as a consequence, the competitive adsorption not only influenced the catalytic activity but also the selectivity or by-products formation. Thus, it should be remarked that the promotion/inhibition effects is generally influenced by the catalysts nature and properties, making it harder to understand and predict the behavior of each VOC in the catalytic oxidation reactions under VOCs mixture conditions [2,20,27].

Hence, the aim of the present work is to better understand the effect of the mixture of two model VOCs like toluene and iPrOH, in their full combustion over MnO_x catalysts supported on MCM-41 and SBA-15. The catalysts were fully characterized and tested in the toluene and iPrOH single oxidation reaction, as well as in the binary mixture oxidation. Moreover, the intermediates production/transformation was evaluated by *in-situ* Diffuse Reflectance Infrared Fourier Transform Spectroscopy (DRIFTS) measurements.

2. Experimental

2.1. Synthesis of catalysts

In this work, 5 wt% Mn supported on two mesoporous ordered silicas was prepared by incipient wetness impregnation method. Firstly, commercial SBA-15 and MCM-41 (XFANO, INC) were pre-treated at 550 °C with a heating ramp of 1 °C min⁻¹ for 4 h in air with a flow rate of 200 mL min⁻¹. In order to measure the support porous volume, 2 g of activated support was placed in a beaker and distilled H₂O was slowly added with a dropper, under continuous stirring, until a homogeneous “moist paste” mixture was formed. The volume of distilled H₂O was measured at this time, which was 7 and 10 mL for SBA-15 and MCM-41, respectively. For the impregnation, the calculated amount of Mn(NO₃)₂·4 H₂O was dissolved in 7 (SBA-15) and 10 mL (MCM-41) of distilled H₂O, the solution was slowly mixed with the activated support until the paste was formed. The paste was dried at room temperature for 24 h, and the collected powder was dried in an oven during 24 h at 100 °C. Finally, the powder was calcined under the same conditions as the pretreated support. The samples were labeled as MnO_x/SBA and MnO_x/MCM.

2.2. Catalysts characterization

The presence of crystalline phases, their identification and chemical composition were evaluated by X-ray diffraction analysis (XRD) using a Bruker D8 Advanced A25 diffractometer, equipped with radiation Cu K α ₁₊₂ (λ = 1.5 Å) and detector LynxEye with 20 from 4° to 80° and using a step of 0.02°. In addition, the crystallite size of the catalysts was calculated using the Scherrer equation.

The manganese oxide particle size distribution was observed by High-Resolution Transmission Electron Microscopy (HRTEM) using a JEOL 2010 LaB6 instrument with an acceleration voltage of 220 kV.

The specific surface area (S_{BET}), total pore volume and average pore diameter were measured by N₂-physisorption at -196 °C using a Belsorp II adsorption measurements apparatus. Previous to adsorption, the catalysts (ca. 300 mg) were degassed at 300 °C under vacuum overnight.

Temperature programmed analyses (H₂-TPR and O₂-TPD) were performed on a TPDRO 1100 equipment (Thermo Scientific) equipped with a thermal conductivity detector (TCD). First, 50 mg of catalysts were pre-treated at 500 °C (10 °C min⁻¹) for 1 h with 40 mL min⁻¹ of 5 % O₂/He and then cooled down to room temperature (RT) under the

same stream. After an Ar purge, the H₂-TPR was carried out by introducing 30 mL min⁻¹ of 5 % H₂/Ar and heating from 30 °C to 900 °C (10 °C min⁻¹). The H₂ consumption was quantified by integration of H₂-TPR profiles. On the other hand, O₂-TPD were done with 50 mg of sample pre-treated with He 30 mL min⁻¹ at 80 °C during 60 min, then cooled down up to 30 °C and exposed to 5 % O₂/He for 60 min. Finally, the sample was heated from 30 to 800 °C during 10 min under He stream at 30 mL min⁻¹.

In order to analyze the chemical states and compositions of the surface elements, X-ray photoelectron spectroscopy (XPS) was applied. The characterization was made on a Kratos Axis Ultra DLD with an X-rays source Al monochromatic (1486.6 eV), 12 kV x 15 mA. All the spectra were recorded from 1200 to 0 eV with an energy pass of 160 eV. High resolution spectra were recorded for the Mn 2p_{3/2}, Mn 2p_{1/2}, O 1s, C 1s and Mn 3s with an energy pass of 40 eV. The charge neutralization was done with a low energy electron beam. All the spectra were calibrated in binding energy by using C 1s (C-C, C-H) photoemission peak at 248.8 eV.

The surface activity, namely Lewis and Brønsted acid sites of the catalysts was investigated by means of pyridine adsorption, as probe molecule, monitored by infrared spectroscopy. IR spectra were collected with a Nexus Nicolet spectrometer equipped with a DTGS detector (Deuterium TriGlyceride Sulfur) and KBr beam splitter. IR spectra were recorded with a resolution of 4 cm⁻¹ and 64 scans. The spectra were normalized to a disc of 10 mg/cm². After activation at 450 °C under synthetic air, the sample was evacuated under dynamic vacuum at 200 °C. Pyridine was thereafter adsorbed (200 Pa at equilibrium) at room temperature. Desorption was performed up to 450 °C, by step of 50 °C. Acidic sites concentrations were obtained using the evolution of the ν_{19b}-absorption mode which allows the quantification of both Brønsted and Lewis sites (at 1548 and 1455–1450 cm⁻¹, respectively), obtained from the surface area of these absorption bands using their molar extinction coefficients (ε_{PyL} = 1.5 cm μmol⁻¹; ε_{PyH+} = 1.8 cm μmol⁻¹ [28]). Acidity was also analysed by Temperature-Programmed Desorption of ammonia (NH₃-TPD). A NICOLET Fourier Transform Infrared analyzer was used to continually monitor the desorbed ammonia. This analyzer was equipped with a heated 2 m gas cell and a DTGS detector. Both catalysts, which were loaded into a U-shaped quartz tube to acquire the NH₃-TPD profiles, were initially pre-treated at 500 °C for 0.5 h in an oxidative environment (10 % O₂, 20 mL min⁻¹, heating rate of 10 °C min⁻¹). After that, 20 mL min⁻¹ of He flow were introduced and the temperature was decreased to 80 °C. At this temperature, a total flow of 40 mL min⁻¹ of 1000 ppm NH₃ was introduced until saturation. After that, the samples were exposed to He for 0.5 h to eliminate the physically adsorbed species. Then, NH₃-desorption step was performed by heating (at 10 °C min⁻¹) from 80 to 400 °C.

2.3. Toluene, 2-propanol (iPrOH) and binary mixture catalytic oxidation

The single VOC and binary mixture oxidation reactions were carried out with 50 mg of catalyst placed into a Pyrex fixed-bed U-shape micro-reactor. The catalysts were previously sieved in the grain size 200–300 μm. Then, the reactor was placed inside a tubular electric furnace and the temperature of the catalytic bed was measured by a K-type thermocouple. The reaction gas containing VOC-He stream was introduced by injecting liquid VOC (toluene, iPrOH or mixture of both VOCs) by using a syringe liquid pump (Harvard Apparatus Elite 11) through an evaporator at 200 °C in order to obtain the desired concentration. Catalytic tests were performed at atmospheric pressure, by performing three consecutive heating cycles, at 2 °C min⁻¹, between room temperature and 400 °C and with the following feeding gas mixtures: toluene/air/He (600 ppm of toluene, 20 vol% O₂), iPrOH/air/He (800 ppm of iPrOH, 20 vol% O₂) or VOCs mixture (600 ppm of toluene and 800 ppm of iPrOH, 20 vol% O₂), with a total flow rate of 200 mL min⁻¹ and a Gas Hourly Space Velocity of 26450 h⁻¹. In this manuscript, the third light-off cycle is shown in each case. The outlet stream gases were monitored by a Mass

spectrometer and a Micro Gas chromatograph Inficon 3000 (SRA Instruments) to quantify the concentration of reactants and products. He was used to calibrate the gas analyzers as an internal standard. Finally, the toluene and iPrOH conversion (X_{C₇H₈} and X_{C₃H₈O}, respectively) were obtained by Eqs. 1 and 2:

$$X_{C_7H_8}(\%) = \frac{[C_7H_8]_{in} - [C_7H_8]_{out}}{[C_7H_8]_{in}} \times 100 \quad (1)$$

$$X_{C_3H_8O}(\%) = \frac{[C_3H_8O]_{in} - [C_3H_8O]_{out}}{[C_3H_8O]_{in}} \times 100 \quad (2)$$

where [C₇H₈]_{in} and [C₃H₈O]_{in} correspond to the inlet concentrations of toluene and iPrOH and [C₇H₈]_{out} and [C₃H₈O]_{out} refer to the respective outlet concentrations.

In addition, the yield of CO₂ from toluene and/or iPrOH oxidation as well as the acetone yield from iPrOH oxidation were calculated by Eqs. 3–5:

$$CO_2 \text{ yield}(\%) = \frac{[CO_2]_{out}}{[C_7H_8]_{in} * 7 + [C_3H_8O]_{in} * 3} \times 100 \quad (3)$$

$$\text{Acetone (C}_3\text{H}_6\text{O) yield}(\%) = \frac{[C_3H_6O]_{out}}{[C_3H_8O]_{in}} \times 100 \quad (4)$$

$$\text{Propylene (C}_3\text{H}_6\text{) yield}(\%) = \frac{[C_3H_6]_{out}}{[C_3H_8O]_{in}} \times 100 \quad (5)$$

where [CO₂]_{out}, [C₃H₆O]_{out} and [C₃H₆]_{out} refer to the outlet concentrations of CO₂, acetone and propylene, respectively.

Finally, the specific and the general reaction rates of toluene or iPrOH per specific surface area or mass unit of catalyst were calculated by the Eqs. 6 and 7.

$$-r_{\text{specific}} \text{ (μmol s}^{-1}\text{m}^{-2}\text{)} = F_{\text{VOC}}^{\text{in}} \times \frac{X_{\text{VOC}}}{m_{\text{cat}} \times S_{\text{BET}}} \quad (6)$$

$$-r \text{ (μmol s}^{-1}\text{g}^{-1}\text{)} = F_{\text{VOC}}^{\text{in}} \times \frac{X_{\text{VOC}}}{m_{\text{cat}}} \quad (7)$$

where F_{VOC}ⁱⁿ is the toluene or iPrOH molar flow in the inlet stream, X_{VOC} is the toluene or iPrOH conversion, set at 10 %, m_{cat} is the mass of catalyst and S_{BET} is the specific surface area determined by N₂-pyrhisorption.

2.4. In-situ diffuse reflectance infrared spectroscopy (DRIFTS) analysis

In-situ DRIFTS experiments were carried out in a spectrometer Nicolet iS50 FT-IR using a praying mantis accessory (HARRICK high temperature test chamber) and liquid N₂-cooled MCT detector with a resolution of 2 cm⁻¹. The spectra were recorded from 1000 to 4000 cm⁻¹. The background spectrum was recorded on pure and dry KBr.

Prior to VOCs adsorption and reactions experiments, the catalysts were pretreated under high-purity He with a flow rate of 40 mL min⁻¹ at 150 °C during 90 min in order to remove the adsorbed water and other surface pollutants. Then, background spectra were collected under the same gas stream (high-purity He) at each work temperature (35, 100, 150, 200 and 400 °C) and systematically deducted from the sample spectra. After that, the adsorption and oxidation measurements were carried out under same reaction conditions as those described in previous section (either toluene, or iPrOH, or both VOCs in air-He gas stream). The spectra were recorded after exposing the catalyst surface to each reaction atmosphere for 1 h, reaching steady-state conditions. Between each isothermal step, a He flush was applied to remove the weakly physisorbed VOC. Note that the He atmosphere (after cleaning the weakly physisorbed VOCs) was maintained during the change from one temperature to another and the VOCs were introduced once the new

temperature was reached. The reported spectra are the result of subtracting from the spectra measured at each temperature during the adsorption and oxidation of VOCs the reference one collected under He flow at the corresponding temperature before any adsorption.

3. Results and discussion

3.1. Characterization of the supported MnO_x catalysts

3.1.1. Physico-chemical, textural and structural properties

The XRD patterns of the supports and MnO_x -supported catalysts are shown in Fig. 1. The Fig. 1a depicts the low-angle XRD diffraction patterns, where well-defined reflections attributed to SBA-15 (at 0.87, 1.5, 1.7 and 2.8° according to PDF-00-049-1712) and to MCM-41 (at 2.2, 3.9, 4.5 and 6.0°, according with the PDF-00-0051-1591) were found. Those reflections are characteristic of the mesoporous hexagonal structure [29, 30]. Wide-angle XRD patterns are also depicted in Fig. 1b. In this angular range, no reflection patterns were observed of SBA-15 and MCM-41. However, after manganese impregnation, well-defined MnO_x diffraction peaks were observed for both MnO_x/SBA and MnO_x/MCM supported catalysts. The catalysts showed a main phase attributed to MnO_2 and, according to the PDF-04-005-4365, it belongs to Pyrolusite. On the other hand, Mn_2O_3 in the form of Bixbyite (PDF 04-007-0856) was also presented in the MnO_x/MCM catalyst. No other phases or

impurities were observed in the XRD diffraction patterns. The Pyrolusite crystallite size was estimated by Scherrer equation based on the peak at 28.6° (Table 1), and MnO_x/SBA catalyst presented a lower crystallite size (7.0 nm) compared with MnO_x/MCM catalyst (12.6 nm). In addition, in the latter catalyst, the Bixbyite (calculated with the peak at 32.7°) phase presented a crystallite size of 15.4 nm.

N_2 adsorption-desorption isotherms of the bare and MCM-supported MnO_x are depicted in the Fig. S1 in Supplementary information. The specific surface area (S_{BET}), total pore volume and the average pore size are summarized in Table 1. As observed in Fig. S1a, all samples exhibited a Type IV isotherm with the characteristic hysteresis of mesoporous materials. Bare SBA-15 and MCM-41 materials showed a S_{BET} of 457 and $1008 \text{ m}^2 \cdot \text{g}^{-1}$, respectively, and a total pore volume of 1.2 and $0.9 \text{ cm}^3 \cdot \text{g}^{-1}$, respectively. It should be noted that, in the case of the MCM support, besides observing a greater initial surface area (vs. SBA), a pronounced decrease of S_{BET} was also observed upon deposition of MnO_x , reaching a final value of $782 \text{ m}^2 \cdot \text{g}^{-1}$, while the final S_{BET} was very similar to that of the bare support in the case of MnO_x/SBA catalyst ($433 \text{ m}^2 \cdot \text{g}^{-1}$). This finding could be ascribed to a higher pore blockage on the outermost surface in the case of the MCM-supported catalyst, correlated with the thinner channels expected in this case with respect to the SBA silica support. Indeed, a very different pore size distribution was confirmed between the two supports, as depicted in Fig. S1b, where the mean pore size was 9 nm for SBA-15 and 2 nm for MCM-41. This hypothesis was also confirmed by the TEM micrographs obtained for the manganese oxides-supported catalysts (Fig. 2). In the case of MnO_x/MCM (Fig. 2a), MnO_x particles agglomerates were clearly observed on the surface of the MCM support, while in the case of MnO_x/SBA catalyst (Fig. 2b), smaller MnO_x particles were found to a higher extent inside the pore channels of the silica support. This is in good agreement with XRD results, where the mean MnO_x crystallite size of MnO_x/SBA catalyst was lower than the pore diameter (Table 1), indicating that a significant part of the oxides particles can be indeed confined in the SBA mesopores, which restrains sintering [31]. This different MnO_x distribution and particle size are in agreement with other studies with catalysts deposited on supports with different pore sizes (e.g. MCM-41 and SBA-15) [32,33]. In these studies, the confinement of catalyst particles into the silica channels was usually linked to a higher catalytic activity due to a higher resistance against sintering and a lower catalyst particle size. However, in the present work, the higher activity will be observed on MCM-41 support (vide infra) and it suggests that the particles located on the outermost surface of the MCM support may be more accessible and active for VOCs oxidation than those deposited in the channels of the SBA. Besides, there are other different properties between both supported MnO_x catalysts that may affect the catalytic activity as shown below, notably the catalyst redox active sites, which are considered as determinant factor for aromatic hydrocarbons oxidation [31,34].

3.1.2. Redox and surface properties

The redox properties of the catalysts have been characterized by H_2 -TPR and O_2 -TPD and the profiles are shown in Fig. 3. In the TPR profiles (Fig. 3a), both catalysts show two main reduction peaks, one sharp peak at around 335 °C and a smaller peak (with c.a. 50 % lower area) at around 430 °C, which could be assigned to the reduction of MnO_2 to

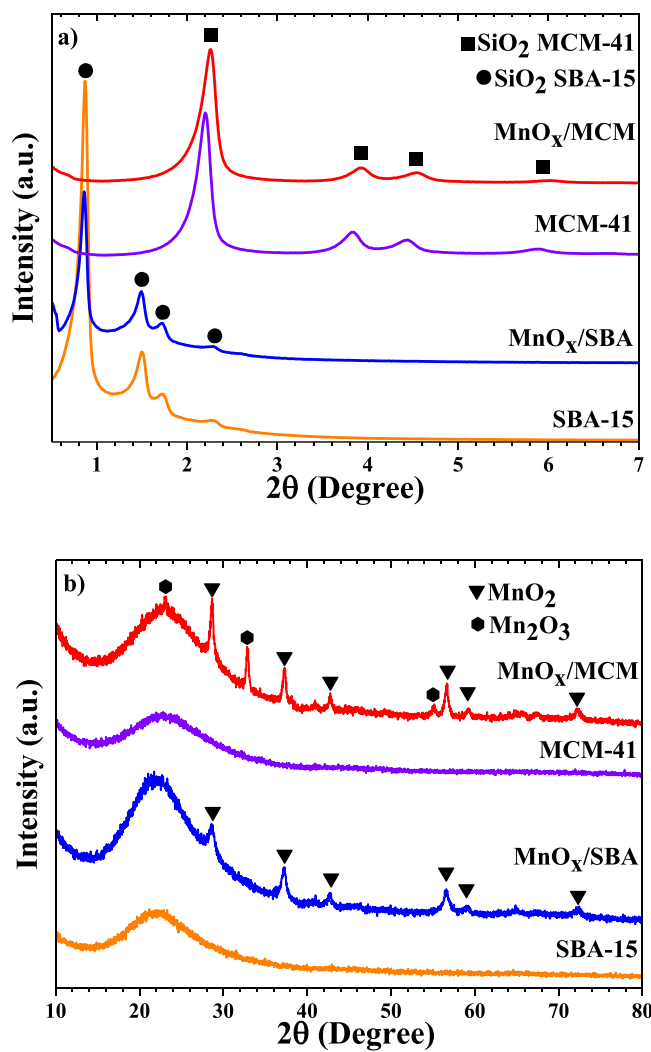


Fig. 1. XRD patterns of MCM-41, SBA-15, and supported MnO_x - catalysts at a) lower angle and b) wide-angle.

Table 1
Textural and structural properties of the SiO_2 and $\text{MnO}_x/\text{SiO}_2$ materials.

Sample	Main phase	Crystallite size (nm)	S_{BET} ($\text{m}^2 \cdot \text{g}^{-1}$)	Total pore volume ($\text{cm}^3 \cdot \text{g}^{-1}$)	Mean pore size (nm)
SBA-15	SiO_2	–	457	1.2	9
MCM-41	SiO_2	–	1008	0.9	2
MnO_x/SBA	Pyrolusite	7.0	433	1.5	9
MnO_x/MCM	Pyrolusite	12.6	782	0.3	2
	Bixbyite	15.4			

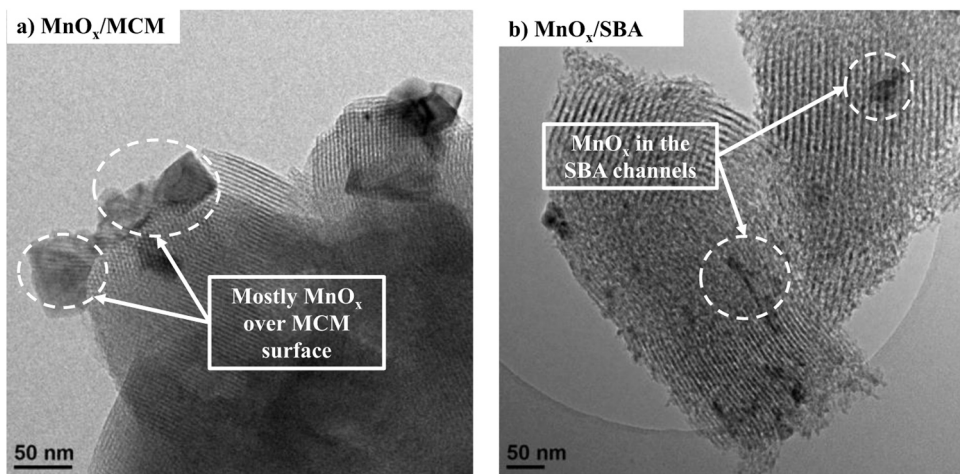


Fig. 2. TEM images of the catalysts synthesized in the present work a) MnO_x/MCM and b) MnO_x/SBA .

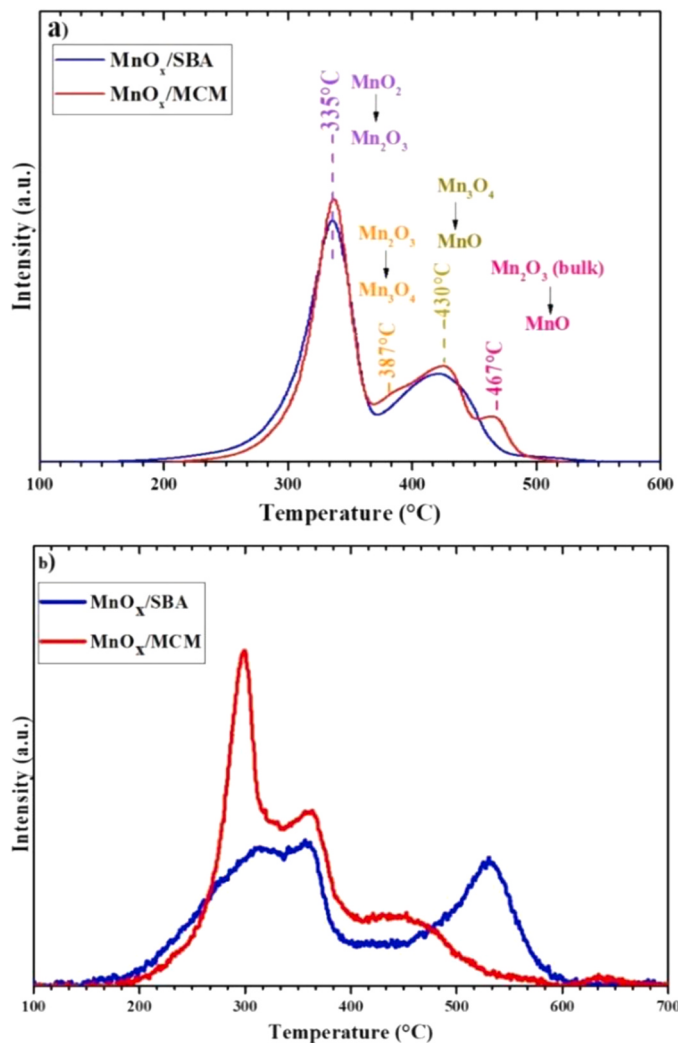


Fig. 3. a) $\text{H}_2\text{-TPR}$ and b) $\text{O}_2\text{-TPD}$ profiles of MnO_x -supported catalysts.

Mn_2O_3 , and the reduction of Mn_3O_4 to MnO , respectively [35]. The intermediate peak that is overlapped at around 387°C could be attributed to the reduction of the formed Mn_2O_3 to Mn_3O_4 according to literature [36]. In addition, a last shoulder was clearly observed on MnO_x/MCM at c.a. 467°C , which has also been attributed to Mn_2O_3 reduction in

literature [37,38]. However, while the peaks obtained at low temperature are typically assigned to highly dispersed MnO_x , in the last small peak, at a temperature close to 500°C , the reduction reaction would be rather attributed to bulk Mn_2O_3 . These multiple peaks were not observed with the MnO_x/SBA catalyst and it could be likely correlated to the identification of a single phase by XRD in this case, as opposed to MnO_x/MCM catalyst, which already presented both MnO_2 and Mn_2O_3 phases since the synthesis. Furthermore, the H_2 consumption has been quantified in the whole temperature range, being very similar in both cases (9.47 and 9.40 $\text{mmol}\cdot\text{g}^{-1}\text{Mn}$ for MnO_x/SBA and MnO_x/MCM , respectively) and, given that the position of the main reduction peaks was not significantly influenced by the support, one can conclude that both catalysts presented similar reducibility.

On the other hand, Fig. 3b shows the $\text{O}_2\text{-TPD}$ profiles obtained for the two catalysts. The oxygen desorption property allows to study the surface oxygen species which, generally strongly affects the catalytic oxidation performance [39,40]. In this work, the manganese oxides catalyst showed mainly two desorption regions, below and above 400°C . In the first one, two main desorption peaks were observed at around 300 and 350°C for both catalysts, although MnO_x/MCM catalyst showed higher intensities. These peaks could be assigned to chemisorbed oxygen surface species, likely O_2 and O^- , respectively [2,41], thus evidencing a higher amount of active oxygen surface species in MnO_x/MCM catalyst. On the other hand, the oxygen desorbed from 400 to 600°C could be attributed to the release of near-surface lattice oxygen, according to several authors [2,39,42,43]. The amount of desorbed oxygen in this region was lower in MnO_x/MCM than in MnO_x/SBA , but the desorption temperature was also lower in the former case, which denotes a better oxygen mobility over the MnO_x/MCM catalyst.

In addition, to investigate the surface elemental composition and chemical states of MnO_x catalysts, XPS analysis was carried out and the corresponding profiles are depicted in Fig. 4. The $\text{Mn } 2p_{3/2}$ and $\text{Mn } 2p_{1/2}$ regions (Binding energy = 670–635 eV) are shown in the Fig. 4a, which were deconvoluted into two peaks corresponding to different Mn oxidation states. The peaks located at 641.6 and 653.1 eV were assigned to Mn^{3+} , while the peaks at 645.2 and 656.7 were attributed to Mn^{4+} [2, 42, 44], respectively. Thus, the corresponding $\text{Mn}^{3+}/\text{Mn}^{4+}$ ratio on the catalyst surface (Table 2) was higher on MnO_x/MCM (5) than on MnO_x/SBA (3), which could indicate that MnO_x/MCM catalyst presented a highest proportion of oxygen vacancies [42,45]. These oxygen vacancies are recognized to be the active sites for oxygen adsorption and activation, favoring the catalytic oxidation of VOCs [2,45]. In addition, after comparing the surface elemental composition by XPS with the bulk analysis by ICP (Table 2), it is clear that the surface Mn content of the MCM-supported catalyst (3.5 wt%) was higher than that of the SBA-supported catalyst (1.1 wt%) while the bulk content obtained from

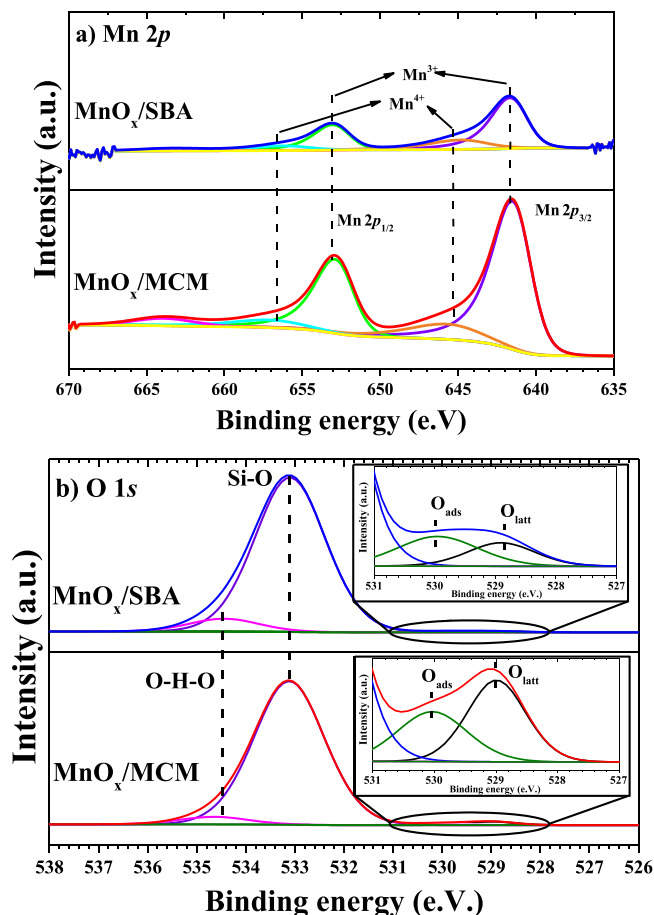


Fig. 4. High-resolution XPS results for MnO_x supported-based catalysts; a) $\text{Mn} 2p$ and b) $\text{O} 1s$.

ICP results was similar in both cases (4.9 and 4.7 wt% for MnO_x/MCM and MnO_x/SBA , respectively). This finding supports the hypothesis of the Mn “loss” in the channels of the SiO_2 supports as noticed by TEM, which was more pronounced in the case of SBA. The lower relative surface content of Mn in the case of MnO_x/MCM was also confirmed by the lower Si/Mn ratio obtained by XPS in this case with respect to MnO_x/SBA (Table 2).

Fig. 4b shows the O 1s spectra (Binding energy around 538–526 eV). Two main peaks were clearly observed at 533.1 and 534.5 eV, attributed to oxygen belonging to the Si–O bond and chemically or physically adsorbed water species, respectively [29,46]. Nevertheless, a less intense peak was also observed at lower binding energies, which can be also deconvoluted in two main peaks as pointed out in zoomed area. Thus, the peak at 528.9 eV was attributed to lattice oxygen (O_{latt}), while the second one at 530.1 eV was attributed to adsorbed oxygen (O_{ads}) [44,47]. In addition, Table 2 shows the O_{latt} and O_{ads} proportions for both supported MnO_x catalysts. It must be noted that the $\text{O}_{\text{ads}}/(\text{O}_{\text{latt}} + \text{O}_{\text{ads}})$ ratio was higher on MnO_x/SBA catalyst than on MnO_x/MCM catalyst. However, the MCM-supported catalyst presented higher amounts of both O_{ads} and O_{latt} compared to those observed on the

SBA-supported catalyst (0.74 and 1.05 vs. 0.52 and 0.31 at% for O_{ads} and O_{latt} , respectively), in agreement with the O_2 -TPD results (Fig. 3b), indicating that MnO_x/MCM catalyst exhibits more active oxygen species on the surface. Indeed, both O_{ads} and O_{latt} surface oxygen species contribute to the VOCs oxidation reaction according to the literature [39,48–51]. Thus, a higher proportion of adsorbed oxygen species, which correspond to the active oxygen species notably at low temperature [52,53], will allow an easier interaction with VOCs, improving the catalytic performance of the catalyst for the oxidation reaction [50,54]. Moreover, the amount of adsorbed oxygen species is currently correlated to the available oxygen vacancies, since gaseous oxygen is commonly adsorbed at these oxygen vacancies [42,51]. Thus, the higher amount of adsorbed oxygen species on MnO_x/MCM surface suggests a higher number of oxygen vacancies, which is in agreement with the higher $\text{Mn}^{3+}/\text{Mn}^{4+}$ ratio presented on MnO_x/MCM catalyst [11]. Thus, these oxygen vacancies will favor an activation of oxygen species, improving the catalyst low-temperature reducibility and, as a consequence, the catalytic activity at low temperature. Moreover, in most of the cases, the oxidation reactions occurred on the surface of MnO_x following the Mars–van-Krevelen (MvK) mechanism [11], which indicates that a high amount of lattice oxygen is also beneficial for the improvement of the catalytic oxidation [6]. All in all, MnO_x/MCM catalyst could present the higher catalytic activity given that presented the higher proportion of O_{ads} and O_{latt} species, which might enhance the VOCs catalytic oxidation.

Pyridine is one of the most used basic probe molecule to characterize the surface acidity of solids [55]. In this study, infrared spectroscopy of adsorbed pyridine was used to determine the influence of the SBA-15 and MCM-41 host supports in the amount and distribution of supported MnO_x catalysts acidic sites. First, free hydroxyl group assignment, reported in Fig. S2, was consistent with the literature and an asymmetric and sharp band at around 3745 cm^{-1} was detected, assigned to isolated silanol groups [28]. Due to the nitrogen electron lone pair, pyridine should interact with acidic centres to form (i) coordinated species on Lewis acid sites (PyL) and (ii) the pyridinium ion on protonic sites (PyH^+), both giving rise to specific ν_{8a} , ν_{8b} , ν_{19a} and ν_{19b} ring (CCN) vibration modes. IR spectra of pyridine desorbed at 150°C are depicted in Fig. S3 to compare the acidic properties of the catalysts. At this temperature, physisorbed and H-bonded pyridine were removed from the surface. Higher amount of acids sites was observed for MnO_x/MCM compared to MnO_x/SBA , which adsorbed virtually no pyridine. Over MnO_x/MCM , adsorption of pyridine mainly gives rise to coordinated PyL species, characterized by bands at 1450–1455, 1492, 1577, 1608 and 1624 cm^{-1} . The appearance of the bands at 1492, 1548 and 1640 cm^{-1} indicates the protonation of pyridine over Brønsted acid sites in low content. Fig. S4 reports the evolution of the Lewis acid sites concentration versus pyridine evacuation. The higher acidity of the MCM-supported catalyst was also verified by NH_3 -TPD measurements. As can be observed in Fig. S5a, three NH_3 desorption peaks were found on MnO_x/MCM catalyst related to weakly, medium and highly acid sites, in increasing direction of temperature, that were negligible in the cases of MnO_x/SBA (Fig. S5b).

3.2. Toluene catalytic oxidation

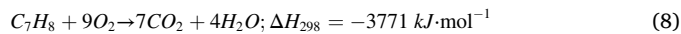
The catalytic performance of the synthesized supported catalysts for toluene oxidation was measured in the range of 100 to 450°C . Fig. 5

Table 2

Bulk and surface elemental analysis of the MnO_x -supported catalysts obtained by ICP-OES and XPS measurements.

Catalyst	ICP-OES		XPS					
	Bulk Mn wt%	Surface Mn wt%	Si/Mn	$\text{Mn}^{3+}/\text{Mn}^{4+}$	Mn ³⁺ at%	Mn ⁴⁺ at%	O_{ads} at%	O_{latt} at%
MnO_x/SBA	4.90	1.1	76.50	3.00	0.30	0.10	0.52	0.31
MnO_x/MCM	4.70	3.5	23.58	5.00	1.05	0.21	0.74	1.05

shows the toluene oxidation light-off curves in terms of a) toluene conversion and b) CO_2 yield. Carbon dioxide and water were the only products detected on the micro-GC and Mass spectrometer instruments, according to reaction (8), without evidence of the formation of CO or any other product. In fact, Fig. 5a and b showed a good correlation between the evolution of toluene conversion and CO_2 yield.



MnO_x/MCM presented slightly higher activation energy (143 kJ mol^{-1}) than MnO_x/SBA (136 kJ mol^{-1}). The global reaction rate, calculated at a toluene conversion of 10 %, was also higher in the former case (48 vs. 40 $\mu\text{mol g}^{-1} \text{s}^{-1}$), which suggest that the specific surface area, which was much higher on the MCM-supported catalyst (Table 1), plays an important role in the catalytic oxidation over MnO_x , in agreement with previous reports [2,45,56]. Indeed, the specific reaction rate (i.e., normalized by S_{BET}) was lower on the MCM-supported catalyst (0.06 vs. 0.09 $\mu\text{mol m}^{-2} \text{s}^{-1}$). However, according to the very different profiles obtained for the light-off curves, the specific surface area was not the only determining parameter. It was clear from Fig. 5 that MnO_x/MCM was more active than MnO_x/SBA at low and intermediate temperatures (up to 370 $^{\circ}\text{C}$). This enhanced catalytic performance

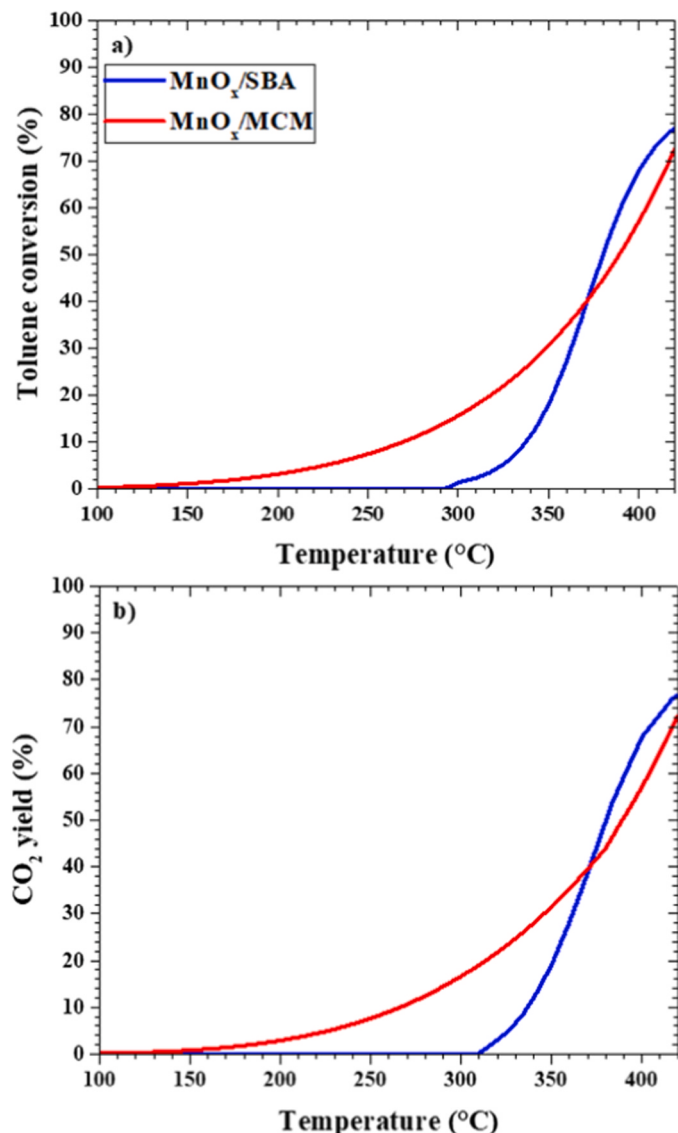


Fig. 5. Single toluene catalytic oxidation over the manganese oxides catalysts: a) light-off curves and b) CO_2 yield as a function of the reaction temperature.

could be associated to the higher concentration of active catalyst on the outermost surface of MCM during the deposition as previously mentioned. Besides, given that toluene oxidation reaction follows a Mars van Krevelen (MvK) mechanism, the higher oxygen mobility and higher surface concentration of adsorbed (O_{ads}) and lattice (O_{latt}) oxygen observed by XPS and O_2 -TPD, likely have a strong impact on the toluene mineralization [39,57].

To investigate the catalytic reaction mechanism of the oxidation of toluene, *in-situ* DRIFTS measurements were also carried out in toluene-air atmosphere at different temperatures between 35 and 400 $^{\circ}\text{C}$ over the MnO_x catalysts. The obtained results are shown in the Fig. 6a and b for MnO_x/MCM and MnO_x/SBA , respectively and the main bands attributed to the toluene molecule and oxidation intermediates are shown in Table 3.

Fig. 6a shows the DRIFTS spectra obtained for the catalytic oxidation of toluene over MnO_x/MCM catalyst. At 35 $^{\circ}\text{C}$, the bands in the range of 3090–2870, 1600, 1494 and 1454 cm^{-1} generally belong to C-H stretching vibration of the benzene ring, and the band at 1291 cm^{-1} may be attributed to the C-H symmetrical vibration of methyl group [6,49,58–62]. These bands evidence the toluene adsorption over the MnO_x/MCM catalyst at low temperature. Furthermore, weaker bands could be observed between 1000 and 1220 cm^{-1} , which could be attributed to benzyl alcohol. Moreover, the band at 1680 cm^{-1} is assigned to $\nu\text{C=O}$ stretching vibrations bands of carboxylates species indicating the formation of benzoates species [59]. These bands indicate

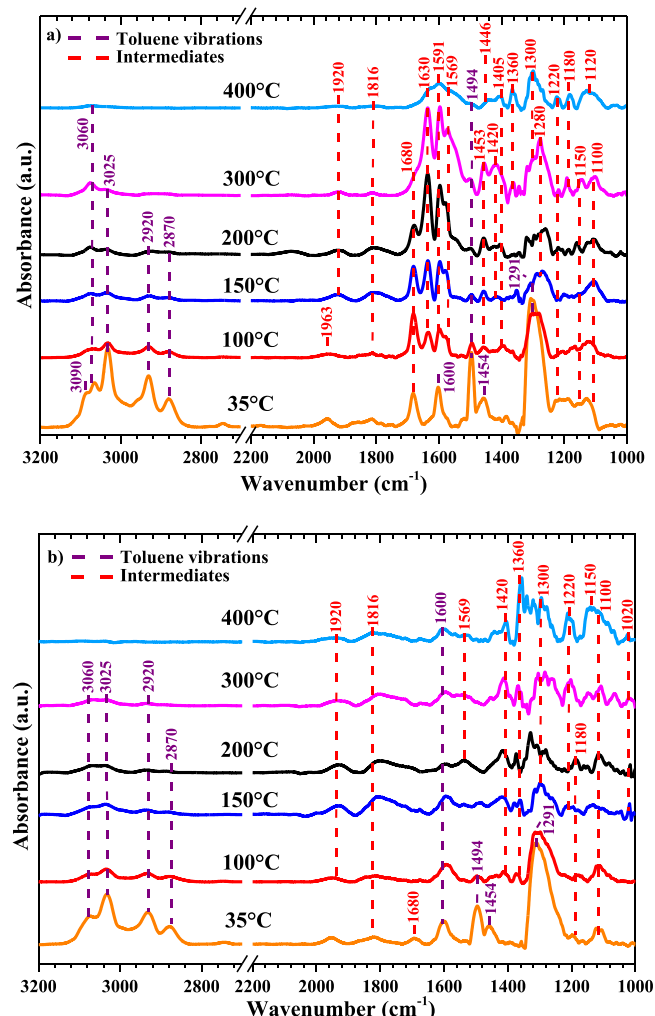


Fig. 6. *In-situ* DRIFTS spectra of the toluene catalytic oxidation over a) MnO_x/MCM and b) MnO_x/SBA catalysts.

Table 3

Main bands of toluene oxidation intermediates.

Position (cm ⁻¹)	Assignment	Reference
Toluene adsorption bands		
3090-2870	Aromatic ring (ν sC-H)	[60,62]
1600	Aromatic ring (ν sC-H)	[62]
1494-1454, 1026	Aromatic ring (ν sC-H)	[2,62]
1291	Methyl group (ν _a CH ₃)	[61]
Reaction intermediates		
2360-2330	CO ₂ (O=C=O)	[69]
1963-1816, 1300	Maleic anhydride (ν C=O)	[48,66]
1680, 1591, 1569, 1420, 1405	Benzoates (ν C=O)	[63,64,69]
1630	Carboxylates species (ν _{as} COO)	[86]
1453, 1448	Benzaldehyde (ν C=O)	[39]
1360, 1280, 1220, 1150-1000	Alkoxide or benzyl alcohol (ν CO-)	[48,68]
1180	Benzoic acid (ν C-O)	[68]

that part of adsorbed toluene interacted with the active oxygen species by abstracting an H of the methyl group at low temperature [60]. Nevertheless, the CO₂ bands formation were not observed. This indicates that toluene oxidation needs more energy to form CO₂, which is in agreement with the light-off toluene oxidation curves where the CO₂ formation started at 150 °C (see Fig. 5b).

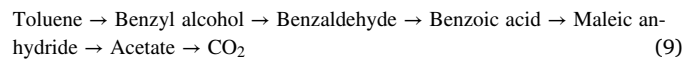
As the temperature raised to 100 °C, the intensity of the aromatic ring and C-H_x species showed a sharp decrease, indicating that the adsorbed toluene was either desorbed or oxidized. The latter hypothesis is supported by an increase observed in the band associated to surface intermediates such as carboxylates species (at 1680 cm⁻¹ [59]), similar to what has been previously shown in the literature [63]. New bands associated to the formation of benzoates (at 1591, 1569 and 1405 cm⁻¹) and other carboxylates species (ν COO stretching vibrations bands at 1630 cm⁻¹) were also observed [60,64,65]. Finally, weak bands were observed at 1453 cm⁻¹, attributed to benzaldehyde, and at 1963 and 1816 cm⁻¹ attributed to maleic anhydrides species [48,66], which indicate the aromatic ring cleavage of the toluene molecule. By increasing the temperature from 100 to 200 °C, the bands attributed to adsorbed toluene further decreased and those related to all toluene reaction intermediates mentioned above increased. Two additional bands also appeared at 1280 and 1100 cm⁻¹, which could be attributed to alkoxide or benzyl alcohol species (ν CO-) [67,68]. In addition, CO₂ bands were observed at 2360 and 2330 cm⁻¹ [69] at temperatures higher than 100 °C (see Fig. S6a), which is in agreement with the toluene mineralization observed in the light-off curves (Fig. 5). Furthermore, at 300 °C most of the bands attributed to intermediates like benzyl alcohol (1280, 1100 cm⁻¹), benzaldehyde or benzoates (1591, 1569, 1453, 1420 and 1360 cm⁻¹) increased and a new band attributed to benzoic acid (1180 cm⁻¹) appeared. Finally, at 400 °C the bands of toluene oxidation intermediates generally decreased. However, the persistence of some intermediate species bands in this spectrum denotes the incomplete toluene combustion at 400 °C, in agreement with the light-off curves (Fig. 5), where toluene conversion was around 60 % at this temperature. Furthermore, CO₂ bands increased with temperature from 150 to 400 °C (Fig. S6a) while no CO bands were observed in any case (2100–1970 cm⁻¹) [70].

Fig. 6b shows the DRIFTS measurements for MnO_x/SBA catalyst. As with the previous catalyst, at 35 °C, the toluene adsorption bands were clearly observed in the range of 3060–2870, 1600, 1494 and 1454 cm⁻¹ assigned to C-H stretching vibration of the benzene ring, along with the band at 1291 cm⁻¹ attributed to the C-H symmetrical vibration of methyl group [6,58–62]. Bands at 1680 cm⁻¹ (C=O in carboxylates species), 1180 cm⁻¹ (benzoic acid) and 1100 cm⁻¹ (benzyl alcohol) were also observed. Based on the intermediates formation, a similar behavior over both supported catalysts was observed, where toluene molecules were firstly adsorbed on the surface of the catalyst. Then, the highly active oxygen species attacked the C-H bond of the methyl group of toluene, thus being oxidized to benzyl alcohol (ν CO-) [69,71]. The latter indicates that toluene is also partially oxidized at

low-temperature over the surface of MnO_x/SBA catalyst. However, the temperature of the catalyst was not enough to deeply mineralized toluene, in agreement with the light-off curves observed in the Fig. 5.

As the temperature increased from 100 °C, the bands at 3090–280, 1600, 1494, 1454 and 1291 cm⁻¹ were progressively less intense and completely disappeared at 400 °C, similarly to MnO_x/MCM catalyst, due to toluene desorption/oxidation reaction. The latter assumption was confirmed by the appearance of intermediates formation bands at 1920, 1816 and 1300 cm⁻¹ attributed to maleic anhydrides (ν C=O) as well as the bands at 1569, 1420 and 1360 cm⁻¹ assigned to benzoate species [39,69] and the bands at 1180 and 1150–1020 cm⁻¹ related to benzoic acid and benzyl alcohol, respectively. These bands progressively increased with the temperature, especially those related to benzoate and maleic anhydrides species, although the temperature effect was less pronounced for this catalyst with respect to MnO_x/MCM. In addition, in the case of MnO_x/SBA catalyst, pronounced CO₂ bands were only clearly observed at temperatures beyond 300 °C (Fig. S6b), in agreement with the light-off curves (Fig. 5). These DRIFTS spectra also confirmed the higher catalytic activity of MnO_x/MCM catalyst with respect to MnO_x/SBA. Indeed, in Fig. 6b, the intermediates bands did not decrease along the studied temperature range (not even at 400 °C), as opposed to MnO_x/MCM catalyst. This denotes a lower activity of MnO_x/SBA catalyst for toluene mineralization in agreement with the right-shift observed in the light-off curve (both toluene conversion and CO₂ yield, Fig. 5).

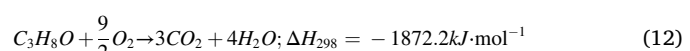
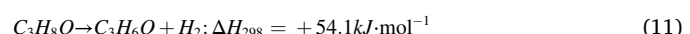
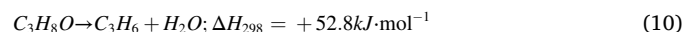
Based on the identified intermediates bands, these *in-situ* DRIFTS measurements allow to propose the following reaction pathway for toluene oxidation, which is similar over both catalysts:



A similar reaction pathway has been reported in the literature [63, 72]. Thus, MnO_x catalysts proved to be active for toluene oxidation and benzoate formation was the one that increased most clearly with the reaction temperature, suggesting that benzoate species were the main toluene reaction intermediate.

3.3. 2-Propanol (iPrOH) catalytic oxidation

In the present work, the iPrOH catalytic oxidation has also been investigated over the supported MnO_x catalysts and the results are shown in the Fig. 7. iPrOH conversion could follow two reaction pathways, either dehydration (reaction 10) or dehydrogenation (reaction 11), depending on the acid or base properties of the catalyst, obtaining as main product propylene or acetone, respectively [49,73,74]. The propylene formation is favored by the dehydration mechanism over acid sites, Brønsted sites being more active than Lewis sites, and by high temperatures [74–79]. On the other hand, acetone formation is produced by the dehydrogenation mechanism, through hydride abstraction, and it takes place over redox and basic sites [2,73,74,80]. Finally, both products can be further oxidized into CO₂ and H₂O leading to the overall iPrOH combustion reaction (reaction 12).



As observed for toluene oxidation, Fig. 7a shows that the MnO_x/MCM catalyst also presented highest catalytic activity for iPrOH conversion than MnO_x/SBA catalyst. As in the case of toluene oxidation, the MCM-supported catalyst showed a higher activation energy (124 vs. 106 kJ mol⁻¹) and a higher global reaction rate at 10 % conversion (48 vs. 39 μmol·g⁻¹ s⁻¹). The enhancement of the catalytic activity could be due to the higher specific surface area, higher amount of surface active

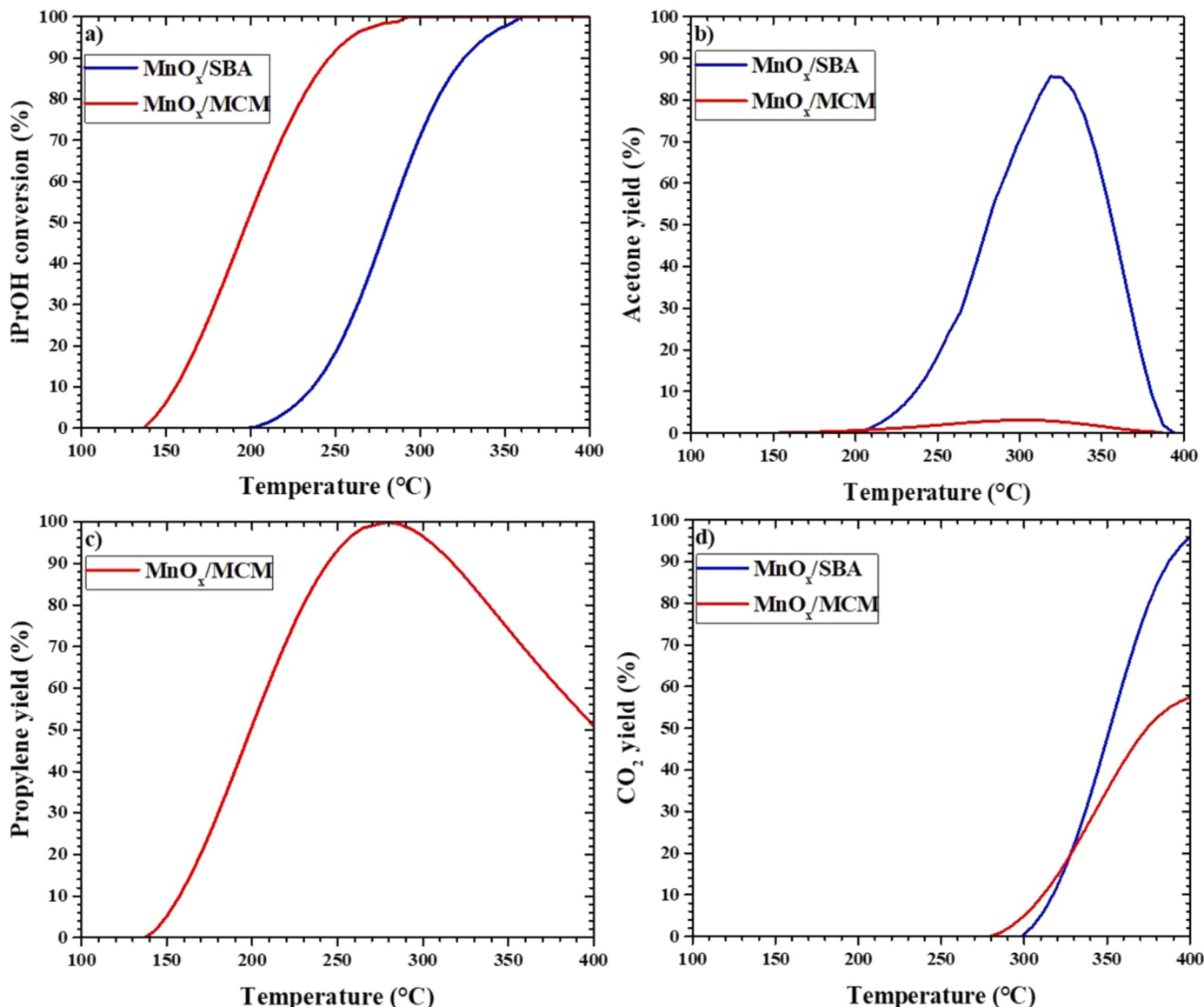


Fig. 7. iPrOH catalytic oxidation over the Mn_2O_3 oxides-based catalysts synthesized by different preparation methods in the present study: a) light-off curves, b) acetone, c) propylene and d) CO_2 yields as a function of the reaction temperature.

oxygen and higher oxygen mobility of the MCM-supported catalyst, as also observed in other studies on VOCs oxidation [2,56,81,82]. Other important difference between the two catalysts was found in Fig. 7b, c. MnO_x/MCM catalyst was very selective for propylene formation, with only little acetone formation. On the contrary, the MnO_x/SBA catalyst was totally selective to acetone, with no propylene detected in this case under the studied reaction conditions. This different behavior can be ascribed to the acidic properties observed in former catalyst, as previously described in Section 3.1.2. MnO_x/MCM presented a much higher amount of acid sites than MnO_x/SBA as determined by the Pyridine-adsorption and NH_3 -TPD measurements (see Figs. S3, S4 and S5). Indeed, this acidity could be related to the Al traces detected by ICP analysis in this catalyst [76], which are not present in SBA-supported catalyst (Table S1). Note that both SBA and MCM mesoporous silicas are commonly assigned as neutral support [33]. According to these results, MnO_x/MCM catalyst mainly performs iPrOH dehydration, while MnO_x/SBA is totally selective for iPrOH dehydrogenation reaction. Regarding CO_2 formation (Fig. 7d), MCM-supported catalyst showed to be more active for iPrOH mineralization than SBA-supported catalyst at temperatures below 330 °C. Other particularity was that propylene was

not fully oxidized at 400 °C, unlike acetone. In this sense, the oxidation temperatures could be likely decreased by using different catalyst synthesis methods or by increasing the content of the active phase in the catalyst (only 4 wt % Mn herein), as found with other catalysts employed in propylene oxidation (e.g., Ag/CeO_2 [83]). On the other hand, the absence of side oxidation products like CO is an advantageous feature of the MnO_x -based catalysts and contrasts with the noble metal catalysts (e.g. $\text{Pt-Pd}/\text{Al}_2\text{O}_3$ [84]), which lead to deactivation phenomena by blockage of catalytic active sites. From the obtained results, one can also suggest that, even with lower activity (evidenced by a higher temperature for full iPrOH conversion), the SBA-supported catalyst seems to be more interesting than the MCM-supported catalyst for a potential practical application of MnO_x -based catalysts for VOCs combustion with pollutant-free CO_2 generation, given the lower temperature required for acetone full oxidation (vs. propylene oxidation).

In-situ DRIFTS measurements were carried out on the supported MnO_x catalysts to better understand the reaction pathways for iPrOH oxidation. The obtained spectra are presented in Fig. 8a and b. The main bands of the reaction intermediates of iPrOH adsorption or transformation are summarized in Table 4.

In Fig. 8a, the bands assigned to iPrOH adsorption over the MnO_x/MCM catalyst were clearly observed in the range of $2969\text{--}2872\text{ cm}^{-1}$. These bands are attributed to asymmetrical and symmetric methyl ($\nu_{\text{s}}\text{CH}_3$) vibration of iPrOH [85]. In addition, the bands located at 1468 and 1384 cm^{-1} are characteristic of asymmetric and symmetric C-H methyl bands (νCH_3), respectively, which could be due to the dissociative iPrOH adsorption [85–87]. Two well defined bands attributed to skeletal ($\delta\text{C-C}$) stretching and methyl (νCH_3) rocking vibrations, respectively, were also observed at 1215 and 1124 cm^{-1} , which are related to the isopropoxide dissociated species due to the adsorption of iPrOH [85,87]. However, the presence of non-dissociative iPrOH species was also evidenced by the band located at 1290 cm^{-1} , which could be attributed to hydroxyl group in isopropoxide species [86]. Thus, the iPrOH adsorption is confirmed at $35\text{ }^\circ\text{C}$ over the MnO_x/MCM catalyst via both dissociative and non-dissociative pathways. According to the literature, the band located at 1711 cm^{-1} could be attributed to acetone (δCH_3) formation. This intermediate could be due to the fast dehydrogenation of iPrOH even at low-temperature [19]. No other intermediates were observed at $35\text{ }^\circ\text{C}$.

By increasing the temperature from 100 to $400\text{ }^\circ\text{C}$, the iPrOH oxidation reaction took place and several reaction intermediates were observed. According to the literature, the reaction mechanism strongly depends on the iPrOH adsorption pathway. The non-dissociative adsorption is usually linked to the dehydrogenation of iPrOH leading to acetone formation [88]. On the other hand, the dissociative iPrOH adsorption leads to the formation of isopropoxy groups and surface

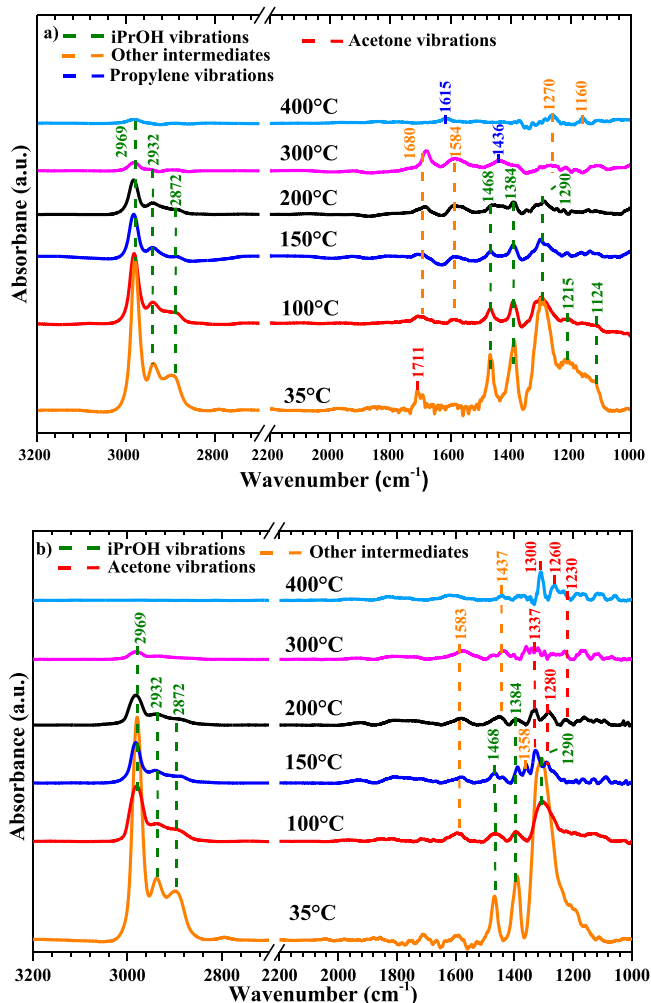


Fig. 8. *In-situ* DRIFTS spectra of the iPrOH catalytic oxidation over a) MnO_x/MCM and b) MnO_x/SBA catalysts.

Table 4
Main bands of iPrOH intermediates.

Position (cm^{-1})	Assignment	Reference
iPrOH adsorption bands		
2969–2872	Methyl vibration ($\nu_{\text{s}}\text{C-H}$)	[85]
1468, 1384	Isopropoxide species (νCH_3)	[85]
1215, 1124	Isopropoxide species ($\delta\text{C-C}$)	[2,85]
1290	Isopropoxide ($\delta\text{O-H}$)	[86]
Reaction intermediates		
2360–2330	CO_2 ($\text{O}=\text{C}=\text{O}$)	[69]
1680, 1584, 1160	Acrylates species ($\nu\text{C=O}$)	[89,92]
1615, 1436	Propylene species ($\nu\text{C=C}$)	[90]
1437	Formates $\nu_{\text{s}}(\text{COO})$	[85,94]
1270	Acrylic acid, ($\nu\text{C-C}$)	[91,92]
1711	Acetone (δCH_3)	[19]
1337, 1300, 1280, 1260, 1230	Acetone ($\nu\text{C-C}$)	[85,87,93]
1583, 1358	Acetate ($\nu_{\text{a,s}}\text{COO}$)	[94]

hydroxyl species, being the iPrOH strongly bonded over the surface Lewis acid sites and giving rise to propylene [85,87]. In the present study, as it happened with toluene adsorption bands, one can observe in Fig. 8a that, at $100\text{ }^\circ\text{C}$, all the bands assigned to iPrOH adsorption sharply decreased (i.e., $2969\text{--}2872\text{ cm}^{-1}$, 1468 , 1384 and 1290 cm^{-1}). Simultaneously, the acetone was either transformed or desorbed at $100\text{ }^\circ\text{C}$ since the band located at 1711 cm^{-1} disappeared. However, new bands raised upon heating, at 1680 and 1584 cm^{-1} , attributed to C=O stretching vibration of acrylate, which could derive from the partial oxidation of propylene [89]. From 150 to $300\text{ }^\circ\text{C}$, the iPrOH adsorption bands located in the range of $2969\text{--}2872$, 1468 , 1384 cm^{-1} progressively decreased, which is in agreement with the light-off curves of catalytic oxidation of iPrOH. According to Fig. 7, both acetone and propylene started to be formed in gas phase at temperatures higher than $150\text{ }^\circ\text{C}$. However, the acetone was not observed at higher temperatures, only the bands at 1680 and 1584 cm^{-1} became stronger which are attributed to acrylate species due to the propylene oxidation. In addition, up to $300\text{ }^\circ\text{C}$, not only the bands related to acrylate formation were observed, but also new bands located at 1436 and 1270 cm^{-1} assigned to propylene [90] and acrylic acid formation [91,92]. Finally, at $400\text{ }^\circ\text{C}$, the iPrOH adsorption bands almost completely disappeared (only a very weak band at 2969 cm^{-1}), as well as the bands at 1680 , 1584 and 1436 cm^{-1} . Acrylate species were the only intermediates remaining (1270 cm^{-1} and a new band at 1160 cm^{-1}) along with some propylene (band at 1615 cm^{-1} , ($\nu\text{C=C}$)) [90], thus suggesting the deep oxidation of iPrOH at this high temperature, in agreement with the light-off curves (Fig. 7d). According to these results, propylene is formed from iPrOH oxidation via dehydration over MnO_x/MCM catalyst. This can be considered as the main intermediate, being subsequently transformed into partial oxygenated compounds. Similar behavior has been reported previously in the literature over Mo-V oxides catalysts [90].

On the other hand, the DRIFTS spectra related to the catalytic oxidation of iPrOH over MnO_x/SBA catalyst are shown in Fig. 8b. At $35\text{ }^\circ\text{C}$, as in the case of MnO_x/MCM catalyst, adsorption bands attributed to iPrOH were observed in the range of $2969\text{--}2872\text{ cm}^{-1}$ attributed to asymmetric and symmetric methyl (νCH_3) vibrations of iPrOH [85]. C-H methyl bands at 1468 and 1384 cm^{-1} , which are characteristic of isopropoxide species due to the dissociative iPrOH adsorption [85–87], were also observed on MnO_x/SBA catalyst surface, as well as a band at 1290 cm^{-1} , attributed to hydroxyl group of non-dissociated iPrOH. However, the latter band is relatively more pronounced in this spectrum with respect to that of MnO_x/MCM catalyst. Besides, in the case of MnO_x/SBA catalyst, no iPrOH intermediates were observed at $35\text{ }^\circ\text{C}$.

By increasing the temperature from 100 to $400\text{ }^\circ\text{C}$, the intensity of the bands attributed to iPrOH adsorption ($2969\text{--}2872$, 1468 , 1384 and 1290 cm^{-1} previously described) decreased, as expected, and several intermediates bands were observed with some differences with respect to MnO_x/MCM catalyst. Acetone formation was evidenced by the bands that appeared at moderate temperatures ($150\text{--}300\text{ }^\circ\text{C}$), in the range of

1337 – 1230 cm^{-1} , attributed to the (vC-C) characteristic vibration of acetone [85,93]. In addition, the band at 1437 cm^{-1} observed from 200 to 400 $^{\circ}\text{C}$ is related to $\nu_s(\text{COO})$ of formate [85,94]. Moreover, the presence of acetate was noticed from 100 $^{\circ}\text{C}$ with the band at 1583 cm^{-1} , which has been assigned on MnO_x/SBA catalyst to acetate $\nu_{\text{as}}(\text{COO})$ formation [94], rather than acrylate species (as identified on MnO_x/MCM spectra), given the absence of the band at 1680 cm^{-1} . The formation of acetate was also confirmed by the band observed at 1358 cm^{-1} at 150 $^{\circ}\text{C}$, attributed to the characteristic vibration, $\nu_s(\text{COO})$, of acetate [95]. In addition, it is important to mention that the CO_2 bands were only observed at temperatures beyond 300 $^{\circ}\text{C}$ (Fig. S7b) on MnO_x/SBA catalyst surface, while they were observed at 200 $^{\circ}\text{C}$ on MnO_x/MCM (Fig. S7a).

According with Fig. 8a and b, two different catalytic pathways were

present depending on the support used. On the MnO_x/MCM catalyst, the reaction was mostly selective to acrylate and carbonate species at low and high temperatures, respectively. These intermediates could be derived from propylene likely formed through a dissociative adsorption mechanism. However, MnO_x/SBA catalyst seemed to undergo mainly iPrOH dehydrogenation to acetone, which also led to acetate and formate species as temperature increased. Accordingly, with these *in-situ* DRIFTS measurements and the light-off curves, the following reaction mechanism can be proposed for MnO_x/MCM (13) and MnO_x/SBA (14) catalysts:

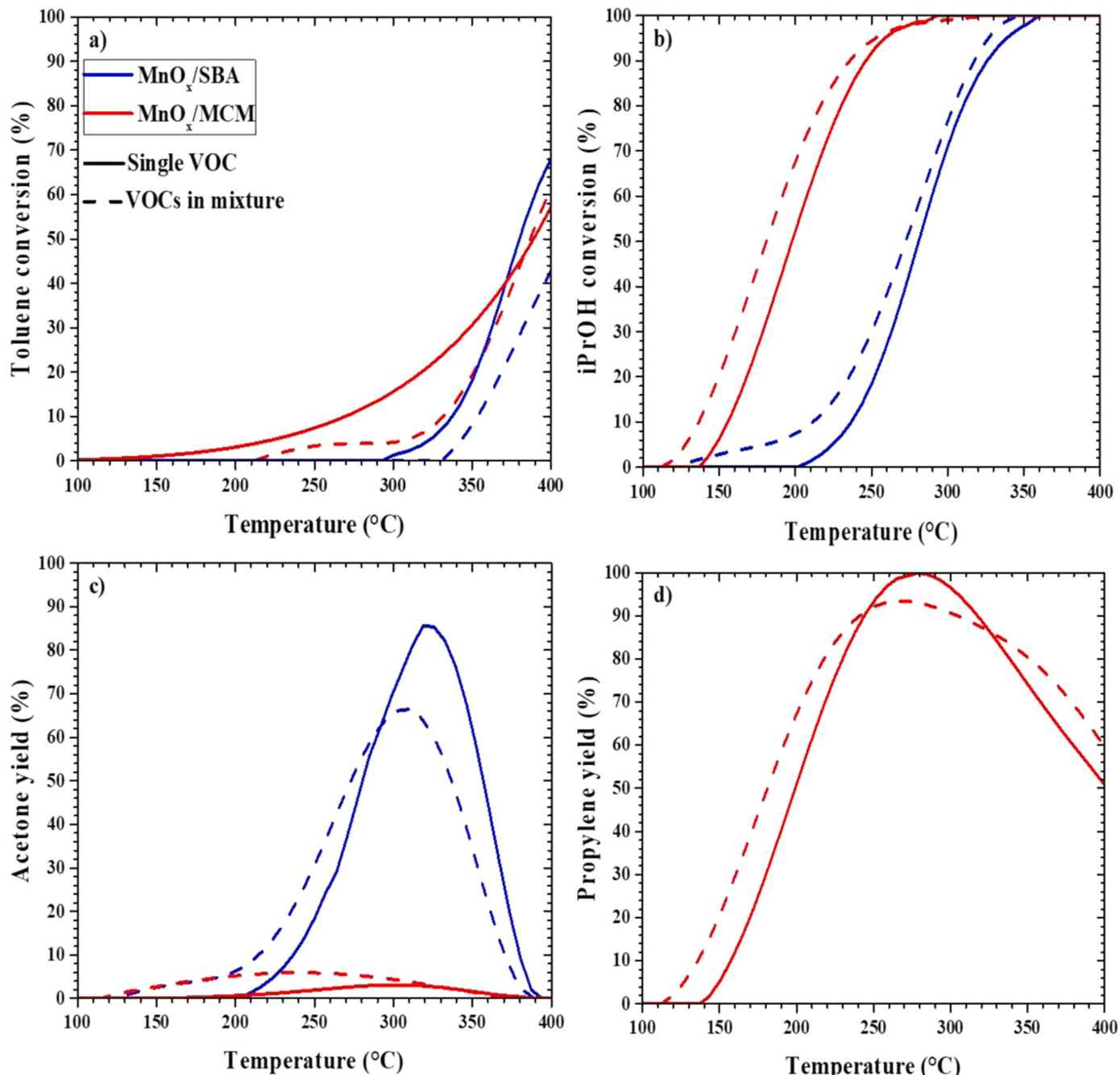


Fig. 9. Comparison between single and binary VOCs mixture oxidation over manganese-oxide catalysts: a) toluene and b) iPrOH conversion as well as the c) acetone, d) propylene yields.

Besides, in both toluene and iPrOH oxidation reactions, *in-situ* DRIFTS measurements proved the higher overall catalytic activity of MnO_x/MCM catalyst with respect to MnO_x/SBA, due to a higher presence of intermediates bands at lower temperatures, and a more pronounced vanishment of these bands at higher temperatures likely associated with a favored mineralization.

The better performance of MnO_x/MCM catalyst can be related to the different properties observed between both ordered mesoporous silicas-supported catalysts. The highest catalytic properties of MnO_x/MCM catalyst could be first attributed to the higher S_{BET} of this catalyst, which translates into a greater quantity of adsorption sites. However, the accessibility of Mn active phase to the silica channels, which was clearly determined by the support pore diameter, was not the determinant factor for VOCs oxidation in this study, and the Mn oxides particles located on the outermost surface of the MCM support seemed to be more active than those deposited in the channels of the SBA. Moreover, the catalyst redox properties play a decisive role for toluene and iPrOH oxidation. Thus, the higher amount of surface Mn and active oxygen species available, including O_{ads} and O_{latt}, on MnO_x/MCM catalyst surface together with a greater oxygen mobility were clearly responsible for the higher performances observed for this catalyst. Moreover, as previously-mentioned, a higher surface Mn³⁺/Mn⁴⁺ ratio, and thus a higher proportion of oxygen vacancies was present on MnO_x/MCM catalyst, which provide active oxygen species for the enhancement of the VOCs catalytic oxidation reaction.

3.4. Toluene and 2-propanol binary mixture oxidation reaction: promotion/inhibition effects

Fig. 9 shows the catalytic performance corresponding to the binary mixture oxidation of toluene and iPrOH over the MnO_x catalysts, in comparison with the previous results obtained under single toluene or iPrOH oxidation conditions. With any of the two VOCs, the catalytic activity was different in the presence of the second one. The toluene oxidation reaction (Fig. 9a) took place at higher temperatures in the binary mixture, which means that toluene oxidation was inhibited by the presence of iPrOH. Moreover, the iPrOH oxidation in the binary mixture reaction was shifted to lower temperature (Fig. 9b), which indicates that the binary mixture favored the iPrOH oxidation. In any case, the most active catalyst for both oxidation reactions was MnO_x/MCM. Thus, these results suggest that the presence of toluene has a promoting effect on the iPrOH oxidation, but iPrOH, being the most reactive VOC due to their higher polarity [22,25], inhibits the toluene oxidation reaction at the VOCs concentration and temperature range studied in this work. To our knowledge, this is the first time that these effects are observed in the literature for silica-based supported MnO_x catalysts. Indeed, although it is very difficult to predict the behavior of VOCs in a mixture, several authors proved that the VOC inhibition/promoting effects depend largely on the catalyst used [2,20,21,23,25–27,96]. For instance, Blasin-Aubé et al. [20], Aguero et al. [23] and Musialik-Piotrowska et al. [96] demonstrated that toluene can have a promoting effect over others VOCs such as ethyl acetate, ethanol and acetone using different MnO_x-based catalysts, while an inhibition effect was pointed out over Pd-zeolites and Pt alumina-based catalysts [21,25,26].

Concerning the effects of toluene over iPrOH oxidation in particular, a promoting effect of toluene over iPrOH partial oxidation, in detriment to the total oxidation, has spotlighted in our previous study over unsupported Mn₂O₃ catalysts [2]. This behavior was attributed to the local exothermicity induced by toluene oxidation [22,24,25] and to the possible decrease of available oxygen for total iPrOH oxidation [97,98]. In the present work, the exothermic effect has also been evidenced in Fig. S8. On both catalysts, when oxidizing either toluene or the VOCs mixture, a slight deviation was observed in the temperature registered inside the reactor with respect to the furnace temperature, thus supporting the hypothesis of the exothermic effect of toluene oxidation, as

one of the plausible reasons for the promoting effect of toluene on iPrOH oxidation under mixture conditions. Note that the enhanced formation of by-products from iPrOH partial oxidation instead of its total oxidation was also observed by Aguero et al. [23] and Musialik-Piotrowska et al. [96] for a mixture of toluene and ethyl acetate or ethanol. The same trend was observed in the present study, where a promotion effect in the by-products formation (i.e., shifted to lower temperatures, Fig. 9c and d) was observed upon VOCs mixture. Note that, as previously observed under single iPrOH oxidation conditions (Fig. 7b and c), the selectivity of the by-products was different depending on the catalyst. MnO_x/SBA catalyst showed a totally selective oxidation of iPrOH to acetone by dehydrogenation, while propylene (by dehydration) and acetone (by dehydrogenation) were observed over the MnO_x/MCM catalyst. It must also be noted that the presence of toluene did not only favoured the acetone formation at lower temperatures, but also its further oxidation to CO₂ at increasing temperatures (there is a left-shift in the acetone yield in the whole temperature range in Fig. 9c). However, in the case of propylene, its formation was promoted by toluene, but its oxidation was inhibited (right-shift at high temperatures in Fig. 9d). One can also observe that the CO₂ formation was inhibited under mixture conditions, since a displacement at high temperatures was observed in the VOCs mixture oxidation compared with the single toluene and iPrOH oxidation reactions (shown in Fig. S9). This behavior suggests that the mixture oxidation reaction promoted the selective formation of partially oxidized by-products such as acetone in the case of MnO_x/SBA and propylene and acetone over MnO_x/MCM catalyst, while the overall VOCs mineralization to CO₂ was unfavored. The mixture inhibition effect on CO₂ generation was more clearly observed in the case of MnO_x/MCM catalyst, since this catalyst presented a significantly higher CO₂ yield at lower temperatures than MnO_x/SBA for single VOC oxidation, while the resultant CO₂ generation under VOCs mixture conditions was very similar on both catalysts. With a view to the commercial application of these MnO_x-based catalysts for VOCs combustion to pollutant-free CO₂, different operation conditions (e.g., increasing O₂ partial pressure) and upgraded catalysts (e.g., optimizing composition, nanostructure) would be necessary, in order to decrease the temperature required for the full oxidation of toluene, iPrOH and the by-products.

Nevertheless, concerning the inhibition/promoting effects of iPrOH over toluene oxidation, only a few studies are reported in the literature [2,25,27], in which an inhibiting effect was never pointed out. For example, Burgos et al. [25], who showed that toluene has a negative impact on the iPrOH oxidation over Pt/Al₂O₃ catalysts, did not observe any effect of iPrOH on the toluene oxidation. Indeed, toluene was oxidized directly from the gas phase with oxygen atoms chemisorbed on Pt. Nevertheless, these authors suggested that the competition between toluene and iPrOH for oxygen atoms did not affect their reactivity. On the other hand, a promoting effect on toluene oxidation in presence of iPrOH was observed in our previous study over unsupported MnO_x [2], which was attributed to both the release of some active sites for toluene adsorption/oxidation and the previously-mentioned exothermic effect generated by the iPrOH/acetone total oxidation. Those effects are therefore opposite to that observed in the present study, where the toluene oxidation seems to be inhibited by the presence of iPrOH over silica-based supported MnO_x catalysts. Nevertheless, Aguero et al. [23] showed that the oxidation of one VOC can be affected by the formation of CO₂ and H₂O derivate from the mineralization of the other VOC presented in the mixture. Thus, the presence of CO₂ and H₂O could inhibit by a adsorption competition the toluene oxidation in the present study, according to the literature [27,99]. Moreover, the preferential adsorption of iPrOH on the catalyst surface due to its higher polarity compared to toluene molecule would delay the adsorption/-transformation of toluene, inhibiting total toluene oxidation at low temperature, as will be demonstrated by *in-situ* DRIFTS measurements in the next section.

In order to better understand the inhibition/promotion effects in the presence of the VOCs mixture (toluene/iPrOH), different *in-situ* DRIFTS

measurements were carried out using the two supported MnO_x catalysts. In the first set of experiments, a mixture of toluene/iPrOH (600 and 800 ppm, respectively) was introduced with air (20 % O_2). The spectra were collected at 35, 100, 150, 200, 300 and 400 $^\circ\text{C}$. Fig. 10a shows the results obtained over MnO_x/MCM catalyst. At low temperature (35 $^\circ\text{C}$), in general terms, a pattern very similar to the one obtained with single iPrOH adsorption (Fig. 8a) was observed. The bands associated to iPrOH adsorption were found in the range of 2969–2872 cm^{-1} [85] as well as some bands at 1468, 1384, 1215 and 1124 cm^{-1} , which are assigned to the dissociative adsorption of iPrOH. Moreover, the band at 1290 cm^{-1} , which is attributed to the hydroxyl group involved in the non-dissociative mechanism, was clearly presented in this spectrum [87]. In addition, acetone formation was also found at 1711 cm^{-1} [19], likely due to the fast dehydrogenation of iPrOH, as previously observed for MnO_x/MCM catalyst on single iPrOH oxidation (shown in Fig. 8a). However, the acetone formation seemed to be more pronounced in the presence of toluene. Moreover, toluene adsorption bands were observed in the range of 3090–2870 cm^{-1} , at 1600 and at 1494 cm^{-1} [6,58–60, 62], although they were negligible with respect to those of iPrOH. However, it should be noted that the main toluene band previously found at 1291 cm^{-1} could be overlapping with that at 1290 cm^{-1} attributed to iPrOH vibration. It is well known that the competitive adsorption of the VOCs over the MnO_x catalysts could affect the adsorption and transformation of both molecules [23,24]. Indeed, the apparently detrimental effect of the mixture on the toluene adsorption was already observed at low temperature with un-supported MnO_x

catalysts in our previous study [2] and can be attributed to the preferential adsorption of iPrOH due to its higher polarity [22,25].

By increasing the temperature, from 35 to 400 $^\circ\text{C}$, the bands associated to iPrOH and toluene adsorption vanished, the latter being undetectable beyond 100 $^\circ\text{C}$. The band attributed to acetone formation (1711 cm^{-1}) also progressively decreased with the temperature. Fig. 10a also shows that the temperature increase led to the formation of some intermediates from both iPrOH and toluene oxidation reactions. The bands at 1680, 1584, 1436 and 1160 cm^{-1} are attributed to propylene and propylene-derived intermediates such as acrylates and carbonates/formates, as previously discussed. Moreover, those at 1300, 1360 and 1220–1020 cm^{-1} can be assigned to maleic anhydrides and alkoxide or benzyl alcohol species, respectively, derived from toluene oxidation. Thus, even if toluene adsorption was hindered by the presence of iPrOH, both VOCs were oxidized on MnO_x/MCM catalyst surface, although toluene oxidation intermediates were detected at higher temperatures than the iPrOH intermediates, in agreement with the observed light-off trends (Fig. 9).

In the case of MnO_x/SBA catalyst (Fig. 10b), at 35 $^\circ\text{C}$, the same bands were found as with MnO_x/MCM catalyst, i.e., iPrOH and toluene adsorption bands and acetone formation at 1711 cm^{-1} . Toluene adsorption bands were again significantly lower than those related to iPrOH adsorption, due to the preferential adsorption of the latter as previously discussed. The main difference between both catalysts at 35 $^\circ\text{C}$ was the absence of bands at 1215–1124 cm^{-1} , which were assigned to dissociative iPrOH adsorption, in the case of MnO_x/SBA . By increasing the temperature from 100 to 400 $^\circ\text{C}$, the bands of both iPrOH and toluene adsorption decreased as expected, and the band at 1711 cm^{-1} vanished. Simultaneously, different bands attributed to acetone, (1300, 1280 and 1239 cm^{-1}), and acetate (1583 and 1358 cm^{-1}) progressively increased up to 300 $^\circ\text{C}$, and above this temperature other bands assigned to formates (1437 cm^{-1}) and toluene-derived intermediates (1360 cm^{-1} and several bands between 1280 and 1100 cm^{-1}) appeared. This is in agreement with the light-off trends of simultaneous toluene and iPrOH oxidation (Fig. 9).

It must be noted that the bands derived from toluene and iPrOH adsorption could be overlapped in many cases since both compounds gave rise to by-products/intermediates with similar functional groups, thus making it difficult the interpretation of the results. However, two general trends can be observed when comparing the spectra obtained with the two catalysts for single VOC oxidation (Figs. 6 and 8) with those obtained in the presence of both VOCs (Fig. 10): i) the higher presence of acetone under mixture conditions, even on MnO_x/SBA catalyst at 35 $^\circ\text{C}$, and ii) the lower bands related to toluene intermediates observed in the presence of iPrOH. This evidences the promoting effect of toluene on the dehydrogenation of iPrOH and the opposite effect of iPrOH on toluene oxidation, as noticed from the catalytic behavior observed above (Fig. 9).

To get more insights about the inhibition/promoting effects in the VOCs mixture oxidation, another experimental approach was also applied. A two-step reaction was performed where toluene and iPrOH were introduced as follows: in the first step either toluene or iPrOH was introduced (in air stream) in the DRIFT cell at low temperature (35 $^\circ\text{C}$) for 30 min. Then, the molecules weakly adsorbed were swept-out by a He flow rate during 15 min. After that, the other VOC (in air stream) was injected continuously for 30 min. DRIFTS spectra were collected under the different VOC atmosphere. Finally, the DRIFT cell was heated at 300 $^\circ\text{C}$ and some spectra were collected at this temperature. The results obtained with MnO_x/MCM catalyst are shown in Fig. 11a and b at 35 and 200 $^\circ\text{C}$, respectively. In Fig. 11a, the “toluene” and “iPrOH” spectra show the pre-adsorption step in each case. Then, in the same figure, the spectrum called “1st toluene, 2nd iPrOH” was obtained after introducing 800 ppm of iPrOH (in air stream) on the toluene-preadsorbed surface during 30 min, and the spectrum called “1st iPrOH, 2nd toluene” was obtained after adding 600 ppm of toluene (in air stream) on the iPrOH-preadsorbed catalyst. The “mixture” profile stands for the respective

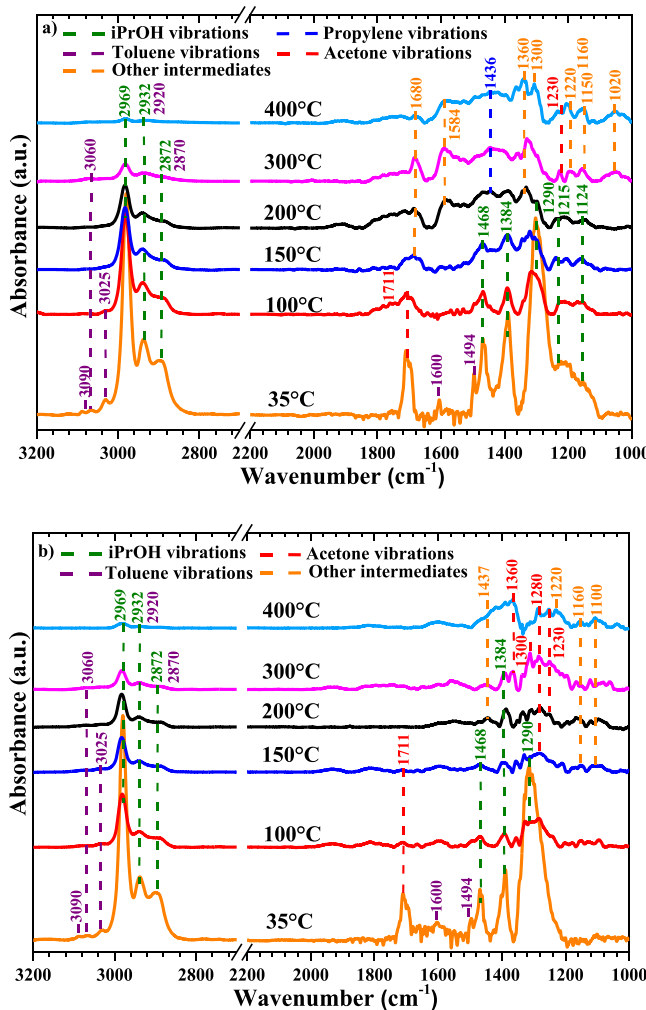


Fig. 10. *In-situ* DRIFTS spectra recorded for mixture oxidation over a) MnO_x/MCM and b) MnO_x/SBA catalysts at different temperatures.

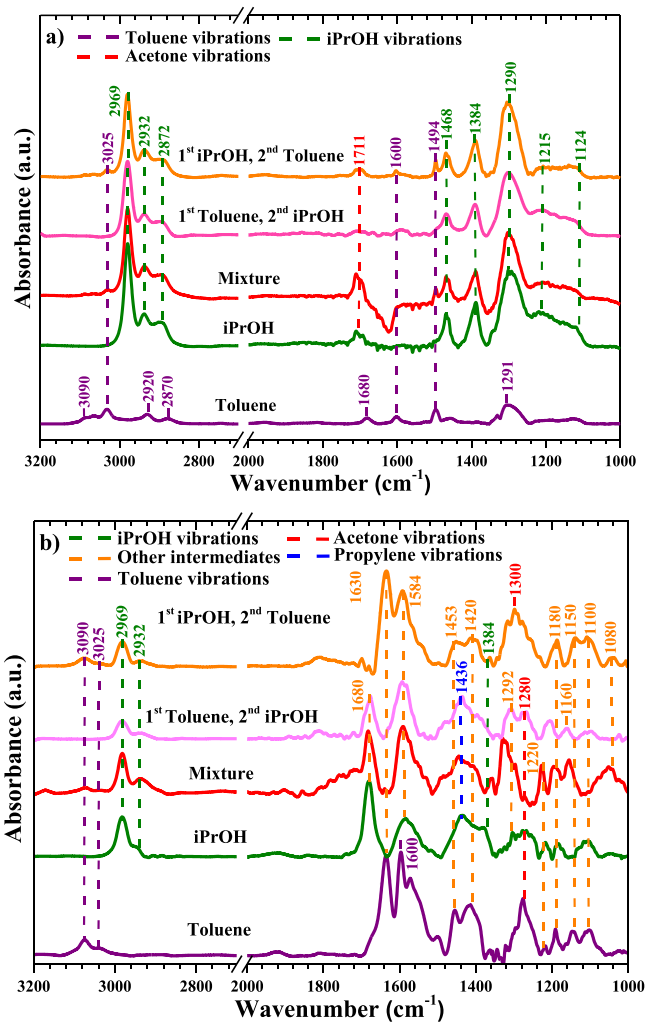


Fig. 11. *In-situ* DRIFTS spectra recorded for single toluene or single iPrOH (first step of the two-step reaction), as well as after continuous adsorption of iPrOH or toluene in the pre-adsorbed VOC at a) 35 °C and b) 300 °C over the MnO_x/MCM catalyst.

spectrum after simultaneously feeding both VOCs at the same conditions during 30 min (which has been shown previously in the manuscript). It can be observed that the profiles of single toluene or single iPrOH were similar to those presented in Figs. 6a and 8a, which demonstrates the experimental reproducibility of the DRIFTS measurements for the MnO_x/MCM catalyst. Note that the bands attributed to toluene and iPrOH were previously described, therefore, those bands will not be described in detail in this section.

When toluene was firstly adsorbed over the MnO_x/MCM catalyst at 35 °C, the main bands of toluene were clearly observed (purple profile in Fig. 11a). However, those bands almost vanished after the adsorption of iPrOH (light-pink profile) and were only slightly observed when iPrOH was firstly adsorbed (orange profile). Moreover, the main bands attributed to dissociative and non-dissociative adsorption of iPrOH (in the range of 2969–2872 cm⁻¹ and those at 1468, 1384, and 1290–1124 cm⁻¹) [85,87] were observed in the presence of iPrOH, before and after the toluene adsorption (olive and orange profiles). However, by comparing the profiles of “1st toluene, 2nd iPrOH”, “1st iPrOH, 2nd toluene” against the “mixture”, it seems that all those profiles are quite similar to the single iPrOH. This great prominence of iPrOH on MnO_x/MCM catalyst is likely linked with its preferential adsorption due to its higher polarity, which is in agreement with the literature [2,22,25]. However, it must be noted that less pronounced

iPrOH adsorption bands were observed after preadsorbing toluene, especially, those bands located at 1462, 1384 and 1290 cm⁻¹. This behavior can be explained by the fact that the pre-adsorption of one VOC will generally have a negative impact, to a greater or lesser extent, on the adsorption of a second VOC. Thus, these *in-situ* DRIFTS measurements at low temperature (35 °C) suggest that the pre-adsorption of toluene could affect the adsorption and transformation of iPrOH. However, the iPrOH was preferentially adsorbed over the MnO_x/MCM catalyst surface, inhibiting the adsorption of toluene.

Fig. 11b shows the DRIFTS spectra obtained after heating at 300 °C on the MnO_x/MCM catalyst. The single toluene, iPrOH and mixture led to the same spectra as those shown in Figs. 6, 8 and 10, respectively. Even though the adsorption of toluene seemed to be inhibited by iPrOH at low temperature, the presence of some bands associated to the toluene adsorption at higher temperature, even in the presence of iPrOH, suggests that this inhibition effect can be considered reversible. Moreover, the formation of toluene intermediates was clearly observed (1630, 1453, 1420, 1280 and 1180–1100 cm⁻¹). Therefore, both adsorption and transformation of toluene were enhanced at high temperature, which could be related to a promoting effect of the temperature on the iPrOH desorption/reaction, releasing active sites for toluene adsorption/oxidation. However, when comparing the spectrum obtained in single-toluene oxidation with that obtained at 300 °C in these new measurements (i.e. two-steps reaction or mixture), the toluene intermediate bands were found to be lower in all those cases in the presence of iPrOH. For example, the bands at 1453, 1420, 1280 and the bands in the range of 1180–1100 cm⁻¹ were less pronounced under consecutive or simultaneous adsorption of both VOCs than under single-toluene oxidation (Fig. 6). This denotes an inhibiting effect of iPrOH on toluene oxidation over MnO_x/MCM catalyst and this effect was especially evident when pre-adsorbing iPrOH, as expected. These DRIFTS findings are in agreement with the toluene oxidation inhibition observed in the light-off curves obtained under mixture conditions in the Fig. 9.

On the other hand, when analyzing the iPrOH intermediates, the co-feeding or pre-adsorption of toluene led to the same bands as those found in the spectrum under single-iPrOH oxidation conditions, and some of them even increased, like the band at 1584 cm⁻¹ (acrylates) and the wide bands found in the region of 1350–1200 cm⁻¹ likely involving several bands related to acetone and isopropoxide. This promoting effect of toluene on iPrOH oxidation also verifies the trends observed in the light-off curves in Fig. 9.

In-situ DRIFTS measurements in the mixture oxidation reaction over the MnO_x/SBA catalyst were also performed and the obtained results at 35 and 300 °C are presented in Fig. 12. As for MnO_x/MCM catalyst, the profiles of single toluene or single iPrOH were similar to those presented in Figs. 6b and 8b, which corroborates the reproducibility of the DRIFTS measurements for MnO_x/SBA catalyst too. Moreover, it can be observed that the pre-adsorption of iPrOH led to a strong decrease of the toluene adsorption bands (Fig. 12a). The most interesting was that the “1st toluene, 2nd iPrOH” profile (light-pink) did not show on this catalyst any iPrOH adsorption as in the case of the MnO_x/MCM catalyst. In this case, with the SBA-supported catalyst, it is clearly observed that toluene pre-adsorption inhibited the iPrOH adsorption. Thus, the toluene pre-adsorbed on MnO_x/SBA surface seemed to cover almost all the available active sites of this catalyst, decreasing or avoiding the subsequent iPrOH adsorption. Nevertheless, as in the case of the MCM-supported catalyst, when iPrOH was firstly adsorbed on MnO_x/SBA (“1st iPrOH, 2nd toluene”, orange profile), toluene still had an influence over the iPrOH since the bands attributed to iPrOH were less pronounced compared with the “mixture” and single-iPrOH (red and olive profiles, respectively) and the bands associated to toluene were presented in both profiles.

At higher temperature (Fig. 12b), as it was also observed on MnO_x/MCM catalyst, the eventual adsorption inhibition effects of one VOC on the other were mitigated. Both toluene and iPrOH adsorption bands were clearly observed, as well as their transformation into the

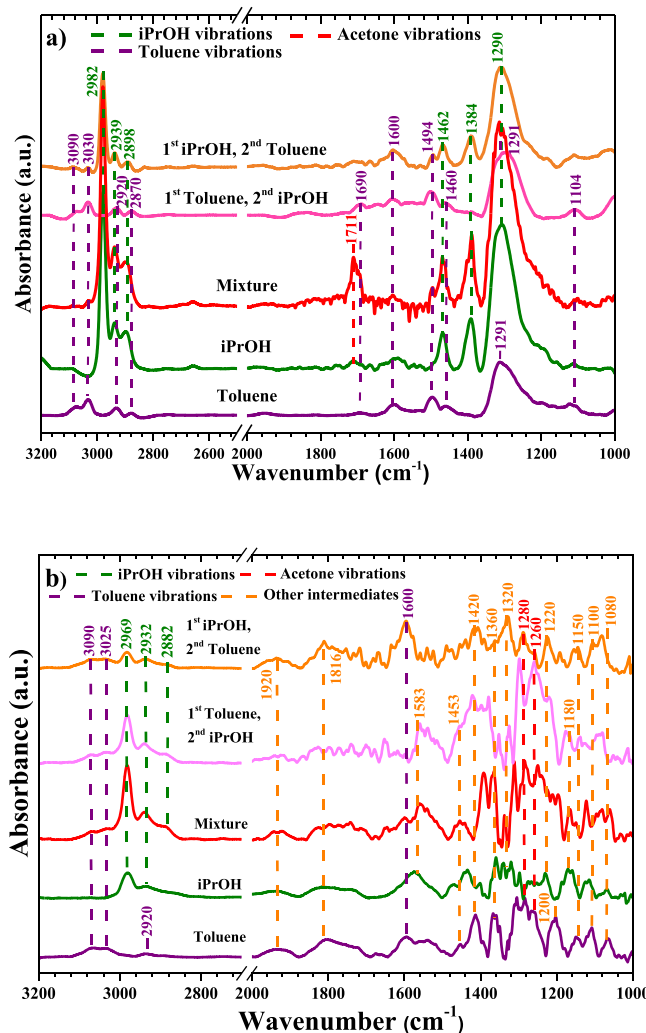


Fig. 12. *In-situ* DRIFTS spectra recorded for single toluene or single iPrOH (first step of the two-step reaction), as well as after continuous adsorption of iPrOH or toluene in the pre-adsorbed VOC at a) 35 °C and b) 300 °C over the MnO_x /SBA catalyst.

previously mentioned intermediates. As with the MnO_x /MCM catalyst, the promoting effect of toluene on iPrOH oxidation and the inhibiting effect of iPrOH on toluene oxidation were also verified on MnO_x /SBA by *in-situ* DRIFTS measurements, although both effects were less clearly observed on this catalyst given its lower catalytic activity and the lower band intensities obtained. For example, in Fig. 12b, one can observe that the bands attributed to carboxylate ($1453, 1360 \text{ cm}^{-1}$) decreased when iPrOH was pre-adsorbed before toluene, while the bands assigned to acetate (1583 cm^{-1}) increased by pre-adsorbing toluene on the catalyst surface.

In summary, according to the *in-situ* DRIFTS measurements, the pre-adsorption of toluene or iPrOH inhibits each other at low temperature, at least partially. MnO_x /MCM catalyst suffered specially the adsorption inhibition effect of iPrOH over toluene and MnO_x /SBA catalyst the opposite. At higher temperatures, it was verified the production of propylene and its derivatives on MnO_x /MCM catalyst and acetone intermediates on both MnO_x /MCM and MnO_x /SBA catalysts. In addition, under VOCs mixture oxidation conditions, the inhibition of toluene oxidation and promotion effect on iPrOH oxidation were confirmed by DRIFTS. Moreover, the reaction mechanism observed in this study changed drastically compared to that supposed by Burgos et al. [25] for a mixture of toluene/ iPrOH over $\text{Pt}/\text{Al}_2\text{O}_3$ catalysts. Indeed, they concluded that the reaction mechanism took place mainly in the gas

phase. However, in this work, each VOC compound was adsorbed on the surface of the catalysts and then reacted with the reactive oxygen, thus competing between each other, which may lead to an improvement of the partial oxidation of one of the VOCs (the case of the promoting effect of toluene on iPrOH) or to the inhibition of the oxidation of the less favorably adsorbed VOC (the case of the inhibition effect of iPrOH on toluene). In addition, as previously-mentioned, the toluene oxidation inhibition by iPrOH could be also attributed to the generated water vapor at high temperatures, which blocks the active sites on the catalyst surface [27,99].

4. Conclusions

Manganese oxides supported on ordered mesoporous silicas such as SBA-15 and MCM-41 were first compared in terms of physico-chemical, redox and surface properties. Their catalytic performances (conversion and selectivity) were then evaluated for the oxidation of single toluene or iPrOH and in a binary mixture of both VOCs. Both supported catalysts presented well-defined MnO_x diffraction peaks mainly attributed to MnO_2 phase. Nevertheless, Mn_2O_3 in the form of Bixbyite was also presented in the MnO_x /MCM catalyst. MnO_x particles were mostly aggregated on the outermost surface of the MCM silica, blocking the small pores (2 nm of average of pore size), whereas they were well-dispersed inside the larger pores of SBA (9 nm). Thus, MnO_x particles located on the outermost surface of the MCM support may be more accessible and active for VOCs oxidation than those deposited in the channels of the SBA. However, there are other different properties between both supported MnO_x catalysts that can affect the catalytic activity. Indeed, MnO_x /MCM catalyst showed the better performance for both toluene and iPrOH oxidation at low and intermediate temperatures (up to 370 °C), which could be attributed to its higher S_{BET} , greater oxygen mobility and higher amount of surface Mn and active oxygen species available, including O_{ads} and O_{latt} . A higher proportion of oxygen vacancies also seemed to be presented on MnO_x /MCM catalyst, which provided active oxygen species to enhance the VOCs catalytic oxidation reaction. Besides, the by-products formed from iPrOH oxidation strongly depended on the support used. MnO_x /SBA catalyst showed a totally selective oxidation of iPrOH to acetone by dehydrogenation, while propylene (by dehydration) was the main product observed over the MnO_x /MCM catalyst, along with minor amount of acetone (by dehydrogenation). This different behavior was ascribed to the acidity observed in latter catalyst. Thus, with a view to the application of MnO_x -based catalysts for pollution-free VOCs combustion, the SBA-supported catalyst seems to be more convenient than the MCM-supported catalyst, at least in the case of iPrOH combustion, given that acetone required a lower temperature to be fully oxidized than propylene. In the binary VOCs mixture oxidation, on the other hand, toluene catalytic activity was hindered by the presence of iPrOH, while iPrOH catalytic oxidation was promoted. Indeed, as confirmed by *in-situ* DRIFTS, iPrOH adsorbed preferentially and hindered toluene adsorption at low temperature range, while at high temperature the inhibiting effect of iPrOH seemed to be related to the water formation after iPrOH mineralization, which could compete with toluene for catalyst adsorption sites. On the contrary, the presence of toluene seemed to favour the iPrOH partial oxidation to acetone or propylene, as well as the acetone full oxidation, while it inhibited the propylene oxidation at high temperature. As a balance, the mixture effect was detrimental for the overall VOCs combustion. This can be attributed to the local exothermicity induced by toluene oxidation and to the possible decrease of available oxygen for total iPrOH oxidation at high temperature. Both, the promoting effect of toluene on iPrOH partial oxidation and the inhibiting effect of iPrOH on toluene oxidation were verified by *in-situ* DRIFTS measurements, based on the adsorbed intermediates observed.

Declaration of Competing Interest

The authors declare the following financial interests/personal relationships which may be considered as potential competing interests: V. Meille reports financial support was provided by PSPC Régions project. If there are other authors, they declare that they have no known competing financial interests or personal relationships that could have appeared to influence the work reported in this paper.

Data Availability

The authors do not have permission to share data.

Acknowledgements

The authors gratefully acknowledge the scientific service and researchers of IRCELYON for the assistance in physico-chemical characterizations and for stimulating discussions and in particular to Pascale Mascunian, Yoann Aizac and Pascal Bargiela. The authors gratefully acknowledge the financial support from BPI France in the framework of the PSPC Régions project "QUALITY AIR" and Ecole Doctorale de Chimie de Lyon.

Appendix A. Supporting information

Supplementary data associated with this article can be found in the online version at [doi:10.1016/j.apcatb.2023.123613](https://doi.org/10.1016/j.apcatb.2023.123613).

References

- [1] M. Piumetti, D. Fino, N. Russo, Mesoporous manganese oxides prepared by solution combustion synthesis as catalysts for the total oxidation of VOCs, *Appl. Catal. B Environ.* 163 (2015) 277–287, <https://doi.org/10.1016/j.apcatb.2014.08.012>.
- [2] E.J. Moreno-Román, J. González-Cobos, N. Guilhaume, S. Gil, Toluene and 2-propanol mixture oxidation over Mn₂O₃ catalysts: study of inhibition/promotion effects by in-situ DRIFTS, *Chem. Eng. J.* 470 (2023), 144114, <https://doi.org/10.1016/j.cej.2023.144114>.
- [3] C. He, J. Cheng, X. Zhang, M. Douthwaite, S. Pattisson, Z. Hao, Recent advances in the catalytic oxidation of volatile organic compounds: a review based on pollutant sorts and sources, *Chem. Rev.* 119 (2019) 4471–4568, <https://doi.org/10.1021/acs.chemrev.8b00408>.
- [4] Y. Guo, M. Wen, G. Li, T. An, Recent advances in VOC elimination by catalytic oxidation technology onto various nanoparticles catalysts: a critical review, *Appl. Catal. B Environ.* 281 (2021), 119447, <https://doi.org/10.1016/j.apcatb.2020.119447>.
- [5] G.R. Parmar, N.N. Rao, Emerging control technologies for volatile organic compounds, *Crit. Rev. Environ. Sci. Technol.* 39 (2008) 41–78, <https://doi.org/10.1080/10643380701413658>.
- [6] C. Yang, G. Miao, Y. Pi, Q. Xia, J. Wu, Z. Li, J. Xiao, Abatement of various types of VOCs by adsorption/catalytic oxidation: a review, *Chem. Eng. J.* 370 (2019) 1128–1153, <https://doi.org/10.1016/j.cej.2019.03.232>.
- [7] L.F. Liotta, Catalytic oxidation of volatile organic compounds on supported noble metals, *Appl. Catal. B Environ.* 100 (2010) 403–412, <https://doi.org/10.1016/j.apcatb.2010.08.023>.
- [8] P. Papaefthimiou, T. Ioannides, X.E. Verykios, Combustion of non-halogenated volatile organic compounds over group VIII metal catalysts, *Appl. Catal. B Environ.* 13 (1997) 175–184.
- [9] C. He, J. Li, J. Cheng, L. Li, P. Li, Z. Hao, Z.P. Xu, Comparative studies on porous material-supported Pd catalysts for catalytic oxidation of benzene, toluene, and ethyl acetate, *Ind. Eng. Chem. Res.* 48 (2009) 6930–6936, <https://doi.org/10.1021/ie900412c>.
- [10] B. Lou, N. Shakoob, M. Adeel, P. Zhang, L. Huang, Y. Zhao, W. Zhao, Y. Jiang, Y. Rui, Catalytic oxidation of volatile organic compounds by non-noble metal catalyst: current advancement and future prospectives, *J. Clean. Prod.* 363 (2022), 132523, <https://doi.org/10.1016/j.jclepro.2022.132523>.
- [11] V. Bratan, A. Vasile, P. Chesler, C. Horoiu, Insights into the redox and structural properties of CoOx and MnOx: fundamental factors affecting the catalytic performance in the oxidation process of VOCs, *Catalysts* 12 (2022), <https://doi.org/10.3390/catal12101134>.
- [12] X. Li, J. Zhang, Y. Zhang, B. Liu, P. Liang, Catalytic oxidation of volatile organic compounds over manganese-based catalysts: recent trends and challenges, *J. Environ. Chem. Eng.* 10 (2022), 108638, <https://doi.org/10.1016/j.jechemeng.2022.108638>.
- [13] T. Lu, F. Su, Q. Zhao, J. Li, C. Zhang, R. Zhang, P. Liu, Catalytic oxidation of volatile organic compounds over manganese-based oxide catalysts: performance, deactivation and future opportunities, *Sep. Purif. Technol.* 296 (2022), 121436, <https://doi.org/10.1016/j.seppur.2022.121436>.
- [14] E. Kantzer, D. Döbber, D. Kießling, G. Wendt, MnO_x/CeO₂-ZrO₂ and MnO_x/WO₃-TiO₂ catalysts for the total oxidation of methane and chlorinated hydrocarbons, *Stud. Surf. Sci. Catal.* 143 (2000) 489–497, [https://doi.org/10.1016/s0167-2991\(00\)80690-4](https://doi.org/10.1016/s0167-2991(00)80690-4).
- [15] C. Zhang, C. Wang, H. Huang, K. Zeng, Z. Wang, H. peng Jia, X. Li, Insights into the size and structural effects of zeolitic supports on gaseous toluene oxidation over MnO_x/HZSM-5 catalysts, *Appl. Surf. Sci.* 486 (2019) 108–120, <https://doi.org/10.1016/j.apsusc.2019.04.201>.
- [16] W. Si, Y. Wang, S. Zhao, F. Hu, J. Li, A Facile Method for in Situ Preparation of the MnO₂ / LaMnO₃ Catalyst for the Removal of Toluene, (2016). <https://doi.org/10.1021/acs.est.5b06255>.
- [17] Y. Cao, C. Zhang, L. Lv, T. Zhang, Y. Chen, S. Tang, Y. Wang, W. Tang, Confinement effect and Hetero-interface enable high-performing MnO_x/CeO₂ oxidation catalysts with exceptional sintering resistance: morphology effect of ceria support, *Chem. Eng. J.* 462 (2023), <https://doi.org/10.1016/j.cej.2023.142257>.
- [18] B. Zhang, L. Zhou, M. Qi, Z. Li, J. Han, K. Li, Y. Zhang, F. Dehghani, R. Liu, J. Yun, Outstanding stability and enhanced catalytic activity for toluene oxidation by Si-O-Mn interaction over MnO_x/SiO₂, *Ind. Eng. Chem. Res.* 61 (2022) 1044–1055, <https://doi.org/10.1021/acs.iecr.1c02504>.
- [19] Z. Wang, P. Ma, K. Zheng, C. Wang, Y. Liu, H. Dai, C. Wang, H.C. Hsi, J. Deng, Size effect, mutual inhibition and oxidation mechanism of the catalytic removal of a toluene and acetone mixture over TiO₂ nanosheet-supported Pt nanocatalysts, *Appl. Catal. B Environ.* 274 (2020), 118963, <https://doi.org/10.1016/j.apcatb.2020.118963>.
- [20] V. Blasins-Aubé, J. Belkouch, L. Monceaux, General study of catalytic oxidation of various VOCs over La_{0.8}Sr_{0.2}MnO_{3-x} perovskite catalyst - influence of mixture, *Appl. Catal. B Environ.* 43 (2003) 175–186, [https://doi.org/10.1016/S0926-3373\(02\)00302-8](https://doi.org/10.1016/S0926-3373(02)00302-8).
- [21] C. He, P. Li, J. Cheng, Z.P. Hao, Z.P. Xu, A comprehensive study of deep catalytic oxidation of benzene, toluene, ethyl acetate, and their mixtures over Pd/ZSM-5 catalyst: mutual effects and kinetics, *Water Air. Soil Pollut.* 209 (2010) 365–376, <https://doi.org/10.1007/s11270-009-0205-7>.
- [22] R. Beauchet, P. Magnoux, J. Mijoin, Catalytic oxidation of volatile organic compounds (VOCs) mixture (isopropanol/o-xylene) on zeolite catalysts, *Catal. Today* 124 (2007) 118–123, <https://doi.org/10.1016/j.cattod.2007.03.030>.
- [23] F.N. Aguero, B.P. Barbero, L. Gambaro, L.E. Cadis, Catalytic combustion of volatile organic compounds in binary mixtures over MnO_x/Al₂O₃ catalyst, *Appl. Catal. B Environ.* 91 (2009) 108–112, <https://doi.org/10.1016/j.apcatb.2009.05.012>.
- [24] T. Pan, H. Deng, Y. Lu, J. Ma, L. Wang, C. Zhang, H. He, Synergistic catalytic oxidation of typical volatile organic compound mixtures on Mn-based catalysts: significant promotion effect and reaction mechanism, *Environ. Sci. Technol.* 57 (2023) 1123–1133, <https://doi.org/10.1021/acs.est.2c06514>.
- [25] N. Burgos, M. Paulis, M. Mirari Antxustegi, M. Montes, Deep oxidation of VOC mixtures with platinum supported on Al₂O₃/Al monoliths, *Appl. Catal. B Environ.* 38 (2002) 251–258, [https://doi.org/10.1016/S0926-3373\(01\)00294-6](https://doi.org/10.1016/S0926-3373(01)00294-6).
- [26] S. Ordóñez, L. Bello, H. Sastre, R. Rosal, F.V. Díez, Kinetics of the deep oxidation of benzene, toluene, n-hexane and their binary mixtures over a platinum on γ -alumina catalyst, *Appl. Catal. B Environ.* 38 (2002) 139–149, [https://doi.org/10.1016/S0926-3373\(02\)00036-X](https://doi.org/10.1016/S0926-3373(02)00036-X).
- [27] G. Rochard, L. Olivet, M. Tannous, C. Poupin, S. Siffert, R. Cousin, Recent advances in the catalytic treatment of volatile organic compounds: a review based on the mixture effect, *Catalysts* 11 (2021), <https://doi.org/10.3390/catal11101218>.
- [28] S. Khabtou, T. Chevreau, J.C. Lavallee, Quantitative infrared study of the distinct acidic hydroxyl groups contained in modified Y zeolites, *Microporous Mater.* 3 (1994) 133–148, [https://doi.org/10.1016/0927-6513\(94\)00015-8](https://doi.org/10.1016/0927-6513(94)00015-8).
- [29] W. Zhong, S.R. Kirk, D. Yin, Y. Li, R. Zou, L. Mao, G. Zou, Solvent-free selective oxidation of toluene by oxygen over MnO_x/SBA-15 catalysts: relationship between catalytic behavior and surface structure, *Chem. Eng. J.* 280 (2015) 737–747, <https://doi.org/10.1016/j.cej.2015.06.051>.
- [30] W.B. Li, M. Zhuang, T.C. Xiao, M.L.H. Green, MCM-41 supported Cu-Mn catalysts for catalytic oxidation of toluene at low temperatures, *J. Phys. Chem. B* 110 (2006) 21568–21571, <https://doi.org/10.1021/jp063580g>.
- [31] Z. Wang, Y. Qin, F. Pan, Z. Li, W. Zhang, F. Wu, D. Chen, W. Wen, J. Li, Mesoporous silica-supported manganese oxides for complete oxidation of volatile organic compounds: influence of mesostructure, redox properties, and hydrocarbon dimension, *Ind. Eng. Chem. Res.* 57 (2018) 7374–7382, <https://doi.org/10.1021/acs.iecr.8b00630>.
- [32] M.H. Amin, Relationship between the pore structure of mesoporous silica supports and the activity of nickel nanocatalysts in the co2 reforming of methane, *Catalysts* 10 (2020), <https://doi.org/10.3390/catal10010051>.
- [33] X. Yu, C.T. Williams, Recent advances in the applications of mesoporous silica in heterogeneous catalysis, *Catal. Sci. Technol.* 12 (2022) 5765–5794, <https://doi.org/10.1039/d2cy0001f>.
- [34] Á. Szegedi, M. Popova, C. Minchev, Catalytic activity of Co/MCM-41 and Co/SBA-15 materials in toluene oxidation, *J. Mater. Sci.* 44 (2009) 6710–6716, <https://doi.org/10.1007/s10853-009-3600-y>.
- [35] G.S. Pozan, Effect of support on the catalytic activity of manganese oxide catalysts for toluene combustion, 124–130, *J. Hazard. Mater.* (2012) 221–222, <https://doi.org/10.1016/j.jhazmat.2012.04.022>.
- [36] S.C. Kim, W.G. Shim, Catalytic combustion of VOCs over a series of manganese oxide catalysts, *Appl. Catal. B Environ.* 98 (2010) 180–185, <https://doi.org/10.1016/j.apcatb.2010.05.027>.
- [37] P.G. Smirniotis, P.M. Sreekanth, D.A. Peña, R.G. Jenkins, Manganese oxide catalysts supported on TiO₂, Al₂O₃, and SiO₂: a comparison for low-temperature SCR of NO with NH₃, *Ind. Eng. Chem. Res.* 45 (2006) 6436–6443, <https://doi.org/10.1021/ie060484t>.

[38] Y. Liu, M. Luo, Z. Wei, Q. Xin, P. Ying, C. Li, Catalytic oxidation of chlorobenzene on supported manganese oxide catalysts, *Appl. Catal. B Environ.* 29 (2001) 61–67, [https://doi.org/10.1016/S0926-3373\(00\)00193-4](https://doi.org/10.1016/S0926-3373(00)00193-4).

[39] X. Lai, X. Zhou, H. Zhang, X. Jiang, T. Lin, Y. Chen, Toluene oxidation over monolithic Mn x / La-Al2O3 catalyst prepared by a CTAB-assisted impregnation method, *Appl. Surf. Sci.* 526 (2020), 146714, <https://doi.org/10.1016/j.apsusc.2020.146714>.

[40] Z. Hou, J. Feng, T. Lin, H. Zhang, X. Zhou, Y. Chen, The performance of manganese-based catalysts with Ce 0.65 Zr 0.35 O 2 as support for catalytic oxidation of toluene, *Appl. Surf. Sci.* 434 (2018) 82–90, <https://doi.org/10.1016/j.apsusc.2017.09.048>.

[41] S. Todorova, J.L. Blin, A. Naydenov, B. Lebeau, H. Kolev, P. Gaudin, A. Dotzova, R. Velinova, D. Filkova, I. Ivanova, L. Vidal, L. Michelin, L. Josien, K. Tenchev, Co3O4-MnOx oxides supported on SBA-15 for CO and VOCs oxidation, *Catal. Today* 357 (2020) 602–612, <https://doi.org/10.1016/j.cattod.2019.05.018>.

[42] J. Jia, P. Zhang, L. Chen, Catalytic decomposition of gaseous ozone over manganese dioxide with different crystal structures, *Appl. Catal. B Environ.* 189 (2016) 210–218, <https://doi.org/10.1016/j.apcatb.2016.02.055>.

[43] M. Wang, L. Zhang, W. Huang, Y. Zhou, H. Zhao, J. Lv, J. Tian, X. Kan, J. Shi, Pt/MnO2 nanosheets: facile synthesis and highly efficient catalyst for ethylene oxidation at low temperature, *RSC Adv.* 7 (2017) 14809–14815, <https://doi.org/10.1039/C6RA26529D>.

[44] X. Yang, X. Yu, M. Lin, X. Ma, M. Ge, Enhancement effect of acid treatment on Mn2O3 catalyst for toluene oxidation, *Catal. Today* 327 (2019) 254–261, <https://doi.org/10.1016/j.cattod.2018.04.041>.

[45] C. Dong, Z. Qu, X. Jiang, Y. Ren, Tuning oxygen vacancy concentration of MnO2 through metal doping for improved toluene oxidation, *J. Hazard. Mater.* 391 (2020), 122181, <https://doi.org/10.1016/j.jhazmat.2020.122181>.

[46] X. Chen, S. Cai, E. Yu, H. Jia, X. Chen, S. Cai, E. Yu, J. Chen, H. Jia, J. Chen, J. Chen, MnO x /Cr 2 O 3 composites prepared by pyrolysis of Cr-MOF precursors containing in situ assembly of MnO x as high stable catalyst for toluene oxidation, *Appl. Surf. Sci.* 475 (2019) 312–324, <https://doi.org/10.1016/j.apsusc.2018.12.277>.

[47] P. Gong, J. Xie, D. Fang, F. He, F. Li, K. Qi, Study on the relationship between physicochemical properties and catalytic activity of Mn2O3 nanorods, *Mater. Res. Express* 4 (2017), <https://doi.org/10.1088/2053-1591/aa9a25>.

[48] X. Yang, X. Yu, M. Jing, W. Song, J. Liu, M. Ge, Defective Mn x Zr 1 – x O 2 solid solution for the catalytic oxidation of toluene: insights into the oxygen vacancy contribution, *ACS Appl. Mater. Interfaces* 11 (2019) 730–739, <https://doi.org/10.1021/acsm.8b17062>.

[49] M. Wang, Z. Wang, S. Liu, R. Gao, K. Cheng, L. Zhang, G. Zhang, X. Min, J. Kang, Q. Zhang, Y. Wang, Synthesis of hierarchical SAPO-34 to improve the catalytic performance of bifunctional catalysts for syngas-to-olefins reactions, *J. Catal.* 394 (2021) 181–192, <https://doi.org/10.1016/j.jcat.2020.08.020>.

[50] J. Deng, S. He, S. Xie, H. Yang, Y. Liu, G. Guo, H. Dai, Ultralow loading of silver nanoparticles on Mn2O3 nanowires derived with molten salts: a high-efficiency catalyst for the oxidative removal of toluene, *Environ. Sci. Technol.* 49 (2015) 11089–11095, <https://doi.org/10.1021/acs.est.5b02350>.

[51] F. Wang, H. Dai, J. Deng, G. Bai, K. Ji, Y. Liu, Manganese oxides with rod-, wire-, tube-, and flower-like morphologies: highly effective catalysts for the removal of toluene, *Environ. Sci. Technol.* 46 (2012) 4034–4041, <https://doi.org/10.1021/es204038j>.

[52] X. Zhang, H. Zhao, Z. Song, W. Liu, J. Zhao, Z. Ma, M. Zhao, Y. Xing, Insight into the effect of oxygen species and Mn chemical valence over MnOx on the catalytic oxidation of toluene, *Appl. Surf. Sci.* 493 (2019) 9–17, <https://doi.org/10.1016/j.apsusc.2019.06.255>.

[53] X.Y. Chen, S.L. Chen, A.P. Jia, J.Q. Lu, W.X. Huang, Gas phase propylene epoxidation over Au supported on titaniosilicates with different Ti chemical environments, *Appl. Surf. Sci.* 393 (2017) 11–22, <https://doi.org/10.1016/j.apsusc.2016.09.159>.

[54] X. Zhang, F. Bi, Z. Zhu, Y. Yang, S. Zhao, J. Chen, X. Lv, Y. Wang, J. Xu, N. Liu, The promoting effect of H2O on rod-like MnCeOx derived from MOFs for toluene oxidation: a combined experimental and theoretical investigation, *Appl. Catal. B Environ.* 297 (2021), 120393, <https://doi.org/10.1016/j.apcatb.2021.120393>.

[55] E.P. Parry, An infrared study of pyridine adsorbed on acidic solids. Characterization of surface acidity, *J. Catal.* 2 (1963) 371–379, [https://doi.org/10.1016/0021-9517\(63\)90102-7](https://doi.org/10.1016/0021-9517(63)90102-7).

[56] X. Zhang, H. Zhao, Z. Song, W. Liu, J. Zhao, Z. Ma, M. Zhao, Y. Xing, Insight into the effect of oxygen species and Mn chemical valence over MnOx on the catalytic oxidation of toluene, *Appl. Surf. Sci.* 493 (2019) 9–17, <https://doi.org/10.1016/j.apsusc.2019.06.255>.

[57] D. Jiang, G. Wan, C.E. García-Vargas, L. Li, X.I. Pereira-Hernández, C. Wang, Y. Wang, Elucidation of the active sites in single-atom Pd1/CeO2Catalysts for low-temperature CO oxidation, *ACS Catal.* 10 (2020) 11356–11364, <https://doi.org/10.1021/acscatal.0c02480>.

[58] P. Wang, J. Zhao, Q. Zhao, X. Ma, X. Du, X. Hao, B. Tang, A. Abudula, G. Guan, Microwave-assisted synthesis of manganese oxide catalysts for total toluene oxidation, *J. Colloid Interface Sci.* 607 (2022) 100–110, <https://doi.org/10.1016/j.jcis.2021.08.170>.

[59] R. Peng, H. Zhang, Y. Guo, W. Huang, Y. Zhang, J. Wu, M. Fu, C. Yu, D. Ye, The lanthanide doping effect on toluene catalytic oxidation over Pt/CeO2 catalyst, *J. Colloid Interface Sci.* 614 (2022) 33–46, <https://doi.org/10.1016/j.jcis.2022.01.071>.

[60] Y. Lyu, C. Li, X. Du, Y. Zhu, Y. Zhang, S. Li, Catalytic oxidation of toluene over MnO2 catalysts with different Mn (II) precursors and the study of reaction pathway, *Fuel* 262 (2019), 116610, <https://doi.org/10.1016/j.fuel.2019.116610>.

[61] C. Zhou, H. Zhang, Z. Zhang, L. Li, Improved reactivity for toluene oxidation on MnOx/CeO2-ZrO2 catalyst by the synthesis of cubic-tetragonal interfaces, *Appl. Surf. Sci.* 539 (2021), 148188, <https://doi.org/10.1016/j.apsusc.2020.148188>.

[62] Z. Wang, S. Xie, Y. Feng, P. Ma, K. Zheng, E. Duan, Y. Liu, H. Dai, J. Deng, Simulated solar light driven photothermal catalytic purification of toluene over iron oxide supported single atom Pt catalyst, *Appl. Catal. B Environ.* 298 (2021), 120612, <https://doi.org/10.1016/j.apcatb.2021.120612>.

[63] Y. Xu, Z. Qu, Y. Ren, C. Dong, Enhancement of toluene oxidation performance over Cu – Mn composite oxides by regulating oxygen vacancy, *Appl. Surf. Sci.* 560 (2021), 149983.

[64] X. Wang, Y. Sun, F. Han, Y. Zhao, Effect of Fe addition on the structure and SCR reactivity of one-pot synthesized Cu-SSZ-13, *J. Environ. Chem. Eng.* 10 (2022), 107888, <https://doi.org/10.1016/j.jece.2022.107888>.

[65] Y. Sun, J. Han, K. Xu, K. Wu, W. Wu, X. Zhang, B. Jiang, Probing the effects of plasma-induced surface species in ring-opening process of toluene decomposition via plasma-excited TPD and in situ DRIFTS, *J. Clean. Prod.* 371 (2022), 133332, <https://doi.org/10.1016/j.jclepro.2022.133332>.

[66] J. Zhong, Y. Zeng, M. Zhang, W. Feng, D. Xiao, J. Wu, Toluene oxidation process and proper mechanism over Co 3 O 4 nanotubes: investigation through in-situ DRIFTS combined with PTR-TOF-MS and quasi in-situ XPS, *Chem. Eng. J.* 397 (2020), 125375, <https://doi.org/10.1016/j.cej.2020.125375>.

[67] P.K. Huttunen, D. Labadini, G. Asselin, S.S. Hafiz, S. Gokalp, M.D. Kipreos, M. Foster, DRIFTS investigation of toluene oxidation on CeO2 nanoparticles, *Surf. Sci.* 720 (2022), 122042, <https://doi.org/10.1016/j.susc.2022.122042>.

[68] P. Wang, J. Wang, J. Zhao, X. Ma, X. Du, S. Peng, X. Hao, B. Tang, A. Abudula, G. Guan, Trace holmium assisting delaminated OMS-2 catalysts for total toluene oxidation at low temperature, *J. Colloid Interface Sci.* (2021), <https://doi.org/10.1016/j.jcis.2021.10.077>.

[69] S.I. Suárez-Vázquez, E.J. Moreno-Román, R. Zanella, A. Cruz-López, C. García-Gómez, A. Nieto-Márquez, S. Gil, Insight into the surface reaction mechanism of toluene oxidation over a composite CeOx/La1-xCexMnO3 catalyst using DRIFTS, *Chem. Eng. Sci.* 259 (2022), <https://doi.org/10.1016/j.ces.2022.117831>.

[70] M.J. Hazlett, W.S. Epling, Mechanistic effects of water on carbon monoxide and propylene oxidation on platinum and palladium bimetallic catalysts, *Catal. Today* 360 (2021) 401–410, <https://doi.org/10.1016/j.cattod.2020.01.024>.

[71] Y. Shen, J. Deng, S. Impeng, S. Li, T. Yan, J. Zhang, L. Shi, D. Zhang, Boosting toluene combustion by engineering Co-o strength in cobalt oxide catalysts, *Environ. Sci. Technol.* 54 (2020) 10342–10350, <https://doi.org/10.1021/acs.est.0c02680>.

[72] H. Sun, Z. Liu, S. Chen, X. Quan, The role of lattice oxygen on the activity and selectivity of the OMS-2 catalyst for the total oxidation of toluene, *Chem. Eng. J.* 270 (2015) 58–65, <https://doi.org/10.1016/j.cej.2015.02.017>.

[73] J.N. Díaz de Leon, A. Cruz-Taboada, Y. Esqueda-Barron, G. Alonso-Nuñez, S. Loera-Serna, A.M. Venezia, M.E. Poisot, S. Fuentes-Moyado, Catalytic dehydration of 2 propanol over Al2O3-Ga2O3 and Pd/Al2O3-Ga2O3 catalysts, *Catal. Today* 356 (2020) 339–348, <https://doi.org/10.1016/j.cattod.2019.05.024>.

[74] J.-L. Dubois, G. Postole, L. Silvester, A. Aurooux, Catalytic dehydration of isopropanol to propylene, *Catalysts* 12 (2022), <https://doi.org/10.3390/catal12101097>.

[75] D. Haffad, A. Chambellan, J.C. Lavalle, Propan-2-ol transformation on simple metal oxides TiO2, ZrO2 and CeO2, *J. Mol. Catal. A Chem.* 168 (2001) 153–164, [https://doi.org/10.1016/S1381-1169\(00\)00516-1](https://doi.org/10.1016/S1381-1169(00)00516-1).

[76] C.P. Nash, A. Ramanathan, D.A. Ruddy, M. Behl, E. Gjersing, M. Griffin, H. Zhu, B. Subramaniam, J.A. Schaidle, J.E. Hensley, Mixed alcohol dehydration over Brønsted and Lewis acidic catalysts, *Appl. Catal. A Gen.* 510 (2016) 110–124, <https://doi.org/10.1016/j.apcata.2015.11.019>.

[77] A. Ghosh, K. Bhaduri, S. Shah, A. Aurooux, J.K. Pandey, B. Chowdhury, Dehydration of isopropanol to propylene over fullerene[C60] containing niobium phosphate catalyst: Study on catalyst recyclability, *Mol. Catal.* 475 (2019), 110470, <https://doi.org/10.1016/j.mcat.2019.110470>.

[78] C.V. Lacerda, A.C.M. Barrios, R.B. Sousa, T.C.C. Franca, R.O.L. Souza, W. A. Gonzalez, N. Essayem, E.R. Lachter, Influence of the support on the catalytic properties of Keggin type heteropolyacids supported on niobia according to two different methodologies: evaluation of isopropanol dehydration and Friedel–Crafts alkylation reaction, *React. Kinet. Mech. Catal.* 124 (2018) 317–334, <https://doi.org/10.1007/s11144-018-1349-5>.

[79] A.M. Alsalme, P.V. Wiper, Y.Z. Khimyak, E.F. Kozhevnikova, I.V. Kozhevnikov, Solid acid catalysts based on H3PW12O40 heteropoly acid: acid and catalytic properties at a gas-solid interface, *J. Catal.* 276 (2010) 181–189, <https://doi.org/10.1016/j.jcat.2010.09.014>.

[80] Z.-J. Gong, C.-C. Chien, S. Mudhulu, J.C.S. Wu, N. Daneu, M.Ma.ček Kržmanc, W.-Y. Yu, SrTiO3 catalysts prepared from topochemical conversion of Bi4Ti3O12 nanoplatelets: surface characterizations and interactions with isopropanol, *J. Catal.* 416 (2022) 222–232, <https://doi.org/10.1016/j.jcat.2022.11.001>.

[81] B. Bai, J. Li, J. Hao, 1D-MnO2, 2D-MnO2 and 3D-MnO2 for low-temperature oxidation of ethanol, *Appl. Catal. B Environ.* 164 (2015) 241–250, <https://doi.org/10.1016/j.apcatb.2014.08.044>.

[82] X. Yang, X. Yu, M. Lin, X. Ma, M. Ge, Enhancement effect of acid treatment on Mn2O3catalyst for toluene oxidation, 0–1, *Catal. Today* (2018), <https://doi.org/10.1016/j.cattod.2018.04.041>.

[83] S. Benissa, L. Cherif-Aouali, S. Hany, M. Labaki, S. Aouad, R. Cousin, S. Siffert, A. Aboukais, Influence of the preparation method and silver content on the nature of active sites in Ag/CeO2 catalysts used for propylene oxidation, *Chem. Phys.* 558 (2022), 111499, <https://doi.org/10.1016/j.chemphys.2022.111499>.

[84] M.J. Hazlett, M. Moses-Debusk, J.E. Parks, L.F. Allard, W.S. Epling, Kinetic and mechanistic study of bimetallic Pt-Pd/Al2O3 catalysts for CO and C3H6 oxidation,

Appl. Catal. B Environ. 202 (2017) 404–417, <https://doi.org/10.1016/j.apcatb.2016.09.034>.

[85] C. Barakat, P. Gravejat, O. Guaitella, F. Thevenet, A. Rousseau, Oxidation of isopropanol and acetone adsorbed on TiO₂ under plasma generated ozone flow: gas phase and adsorbed species monitoring, Appl. Catal. B Environ. 147 (2014) 302–313, <https://doi.org/10.1016/j.apcatb.2013.09.008>.

[86] H. Zhang, L. Dai, Y. Feng, Y. Xu, Y. Liu, G. Guo, H. Dai, C. Wang, C. Wang, H.C. Hsi, H. Huang, J. Deng, A resource utilization method for volatile organic compounds emission from the semiconductor industry: selective catalytic oxidation of isopropanol to acetone Over Au/α-Fe2O3 nanosheets, Appl. Catal. B Environ. 275 (2020), 119011, <https://doi.org/10.1016/j.apcatb.2020.119011>.

[87] F.M. Bkangmo Kontchouo, K. Sun, C. Li, Z. Fu, S. Zhang, L. Xu, X. Hu, Steam reforming of acetone and isopropanol: Investigation of correlation of ketone and alcohol functional groups with properties of coke, J. Energy Inst. 101 (2022) 32–44, <https://doi.org/10.1016/j.joei.2021.12.001>.

[88] S.Y. Liu, S.M. Yang, Complete oxidation of 2-propanol over gold-based catalysts supported on metal oxides, Appl. Catal. A Gen. 334 (2008) 92–99, <https://doi.org/10.1016/j.apcata.2007.09.037>.

[89] A. Ruiz, B. van der Linden, M. Makkee, G. Mul, Acrylate and propoxy-groups: contributors to deactivation of Au/TiO₂ in the epoxidation of propene, J. Catal. 266 (2009) 286–290, <https://doi.org/10.1016/j.jcat.2009.06.019>.

[90] P. Concepción, P. Botella, J.M.L. Nieto, Catalytic and FT-IR study on the reaction pathway for oxidation of propane and propylene on V- Or Mo-V-based catalysts, Appl. Catal. A Gen. 278 (2004) 45–56, <https://doi.org/10.1016/j.apcata.2004.09.024>.

[91] E. Finocchio, G. Busca, V. Lorenzelli, R.J. Willey, FTIR studies on the selective oxidation and combustion of light hydrocarbons at metal oxide surfaces. Propane and propene oxidation on MgCr₂O₄, J. Chem. Soc. Faraday Trans. 90 (1994) 3347–3356, <https://doi.org/10.1039/FT9949003347>.

[92] V.S. Escribano, G. Busca, V. Lorenzelli, Fourier transform infrared spectroscopic studies of the reactivity of vanadia-titania catalysts toward olefins. 2. Ethylene, J. Phys. Chem. 94 (1990) 8945–8950, <https://doi.org/10.1021/j100389a018>.

[93] Y.Y. Li, W.P. Zhang, J. Zhao, K. Wu, H. Xiao, J.R. Li, Highly efficient acetone oxidation over homogeneous Mn-Al oxides with enhanced OMS-2 active phase, Mol. Catal. 537 (2023), 112952, <https://doi.org/10.1016/j.mcat.2023.112952>.

[94] M.D. Hernández-Alonso, I. Tejedor-Tejedor, J.M. Coronado, M.A. Anderson, J. Soria, Operando FTIR study of the photocatalytic oxidation of acetone in air over TiO₂-ZrO₂ thin films, Catal. Today 143 (2009) 364–373, <https://doi.org/10.1016/j.cattod.2009.02.033>.

[95] M.D. Hernández-Alonso, I. Tejedor-Tejedor, J.M. Coronado, M.A. Anderson, Operando FTIR study of the photocatalytic oxidation of methylcyclohexane and toluene in air over TiO₂-ZrO₂ thin films: Influence of the aromaticity of the target molecule on deactivation, Appl. Catal. B Environ. 101 (2011) 283–293, <https://doi.org/10.1016/j.apcatb.2010.09.029>.

[96] A. Musialik-Piotrowska, K. Syczewska, Combustion of volatile organic compounds in two-component mixtures over monolithic perovskite catalysts, Catal. Today 59 (2000) 269–278, [https://doi.org/10.1016/S0920-5861\(00\)00293-5](https://doi.org/10.1016/S0920-5861(00)00293-5).

[97] W. Xu, D. Raftery, J.S. Francisco, Effect of irradiation sources and oxygen concentration on the photocatalytic oxidation of 2-propanol and acetone studied by in situ FTIR, J. Phys. Chem. B. 107 (2003) 4537–4544, <https://doi.org/10.1021/jp025995h>.

[98] T. Yan, J. Gong, C.B. Mullins, Oxygen exchange in the selective oxidation of 2-butanol on oxygen precovered Au(111), J. Am. Chem. Soc. 131 (2009) 16189–16194, <https://doi.org/10.1021/ja9062986>.

[99] F.N. Aguero, A. Scian, B.P. Barbero, L.E. Cadús, Influence of the support treatment on the behavior of MnO_x/Al 2O₃ catalysts used in VOC combustion, Catal. Lett. 128 (2009) 268–280, <https://doi.org/10.1007/s10562-008-9695-y>.